

Split Ring Resonator Design for Agricultural Based Applications

A thesis submitted in partial fulfillment of the requirements for the degree of Master of Science in
Electrical Engineering

By

Joshua David Compaleo
B.S.E.E., Wright State University, 2015

2015

Wright State University

WRIGHT STATE UNIVERSITY

GRADUATE SCHOOL

December 11, 2015

I HEREBY RECOMMEND THAT THE THESIS PREPARED UNDER MY SUPERVISION BY Joshua Compaleo ENTITLED Split Ring Resonator Design for Agricultural Based Applications BE ACCEPTED IN PARTIAL FULFILLMENT OF THE REQUIREMENTS FOR THE DEGREE OF Master of Science In Electrical Engineering.

Michael Saville, Ph.D.
Thesis Director

Brian D. Rigling, Ph.D.
Chair, Department of
Electrical Engineering

Committee on
Final Examination

Michael Saville, Ph.D.

Fred D. Garber, Ph.D.

Yan Zhuang, Ph.D.

Robert E. W. Fyffe, Ph.D.
Vice President for Research and
Dean of the Graduate School

ABSTRACT

Compaleo, Joshua David. M.S.E.E., Department of Electrical Engineering, Wright State University, 2015. Split Ring Resonator Design for Agricultural Based Applications.

Recent advances with manufactured electromagnetic materials known as metamaterials are paving the way to use microwave technology in agricultural development and harvesting. It has been proposed that split ring resonators could be placed on the surface of fruit or vegetables such that the resonant behavior may be monitored and used to estimate the ripeness level. The method is non-destructive and could enable monitoring of large quantities of produce or even be tailored to hand-held devices for consumers.

However, the understanding of corresponding changes in the proposed device's resonant behaviors and ripeness levels are limited. In addition, fruit and vegetables are highly lossy at microwave frequencies making it difficult to establish resonant behavior. Here, the split ring resonator design is studied to determine which design parameters are most influential on maintaining a resonant behavior in the presence of highly lossy media. The results show that for small array sizes, the radial spacing between the rings and the radial widths of the microstrip rings have the most significant influence. However, resonance is only achievable in the presence of low to moderate loss levels. The results also suggest that a large array of resonators may be sufficient to maintain resonance at the loss levels of certain fruit.

Contents

1	Introduction	1
1.1	Motivation	1
1.2	Challenges	3
1.3	Research Hypothesis	4
2	Literature Review	6
2.1	Chapter Overview	6
2.2	Silk-Based Sensing	6
2.3	Split-Ring Resonator Design	7
2.4	Resonance	10
2.5	Dielectric Resonant Antenna	13
2.6	Utilizing Parallel Plate Capacitance to Determine Banana Ripeness	14
2.7	Dielectric Properties of Fruit	15
2.8	Electromagnetic Modeling and Simulation	18
2.9	Finite Element Method in Comsol Multiphysics®	19
2.10	Comsol Multiphysics®	20
3	Methodology	22
3.1	Chapter Overview	22
3.2	Analysis Method	22
3.3	Split-Ring Resonator Equivalent Circuit Model	24
3.4	Wave Equation in a Lossy Medium	26
3.5	Model Validation	28
4	Results	31
4.1	Results	31
4.1.1	Results for a lossless substrate	32

4.1.2	Results for a lossy free space substrate	34
4.1.3	Results for a highly lossy dielectric substrate	35
4.2	SRR Parameter Changes	38
4.2.1	Results for changing gap distance g	38
4.2.2	Results for three split rings	43
4.2.3	Results for changing split width d	44
4.2.4	Results for changing ring width w	46
4.2.5	Summary of geometric changes	47
4.3	Array Size Effects on Resonance	49
4.3.1	Effects of array size on a standard SRR	49
4.3.2	Increasing the gap width on a 4x4 array	50
5	Conclusion and Future Work	52
5.1	Summary	52
5.2	Recommendation for Future Work	53
	REFERENCES	54

List of Figures

1	Conceptual RFID design	2
2	Notional Resonant Curve	3
3	Split-ring resonator electrical parameters.	9
4	SRR array excited with an 8 GHz plane wave.	9
5	Normalized reflection coefficient vs. frequency for varying gap widths w	10
6	Series RLC circuit from [5]	11
7	Input impedance magnitude vs. frequency from [5]	13
8	Dielectric constant as a function of frequency from [9].	17
9	Dielectric loss factor as a function of frequency from [9].	18
10	Geometry for boundary conditions and wave equations for each material.	21
11	Split-ring resonator parameters.	23
12	SRR equivalent circuit model from [26].	24
13	Split width d vs. normalized frequency with simulated data and data from [25].	29
14	SRR model created in Comsol Multiphysics [®]	29
15	Standard SRR configuration	32
16	Normalized SRR reflection vs. frequency with increasing dielectric constant of substrate.	32
17	Normalized SRR transmission vs. frequency with increasing dielectric constant of substrate.	33
18	Normalized SRR reflection vs. frequency with increasing substrate loss factor.	34
19	Normalized SRR transmission vs. frequency with increasing substrate loss factor.	35
20	Normalized SRR reflection vs. frequency with increasing substrate $\text{real}(\epsilon_r)$	36
21	Normalized SRR reflection vs. frequency with increasing substrate $\text{teal}(\epsilon_r)$	36
22	Normalized SRR reflection vs. frequency with increasing substrate $\text{imag}(\epsilon_r)$	37
23	Normalized SRR reflection vs. frequency with increasing substrate $\text{imag}(\epsilon_r)$	37
24	Normalized SRR reflection vs. frequency with increasing substrate $\text{Imag}(\epsilon_r)$	38

25	SRR configuration with increased gap distance g	39
26	Normalized SRR reflection vs. frequency with increasing gap distance g	39
27	Normalized SRR reflection vs. frequency with increasing gap distance g	40
28	Normalized SRR reflection vs. frequency with increasing substrate $\text{imag}(\epsilon_r)$ and $g = 0.7$ mm.	41
29	Normalized SRR reflection vs. frequency with increasing substrate $\text{imag}(\epsilon_r)$ and $g = 0.9$ mm.	41
30	Normalized SRR reflection vs. frequency with increasing substrate $\text{imag}(\epsilon_r)$	42
31	Normalized SRR reflection vs. frequency with increasing gap distance g	43
32	SRR configuration with third inner ring	44
33	Normalized SRR reflection vs. frequency with third inner ring.	44
34	SRR configuration with increased split width d and increased gap distance g	45
35	Normalized SRR reflection vs. Frequency with increasing split width d	45
36	Normalized SRR reflection vs. frequency with decreasing inner ring width r_2	46
37	Normalized SRR reflection vs. frequency with increasing outer ring width r_1	47
38	Normalized SRR reflection vs. frequency with increasing substrate thickness t	48
39	Normalized SRR reflection vs. frequency with increasing substrate $\text{imag}(\epsilon_r)$	48
40	Normalized SRR reflection vs. frequency with increasing array size.	49
41	Normalized SRR reflection vs. frequency with increasing array size and $\epsilon_r = (1 - 3j)$	50
42	Normalized SRR reflection vs. frequency with increasing gap distance g	50

List of Tables

1	Dielectric fruit properties from [9], $\text{real}(\epsilon_r)$	17
2	Dielectric Fruit properties from [9], $\text{imag}(\epsilon_r)$	17

ACKNOWLEDGEMENT

I would like to thank my thesis advisor, Dr. Michael Saville who over the last three years has went out of his way countless times to provide guidance and assistance that allowed me to reach my professional goals. I would also like to thank my senior design partner Carl Gross, for assisting in the Comsol model design and Aaron Retter for creating some of the figures in this thesis.

Dedicated to

I dedicate this thesis to Karen and Pete Compaleo for placing the bar so unbelievably high. For being the best support system that anyone could ask for and for selflessly making so many sacrifices so I will never have to. I love you mom and dad.

1 Introduction

1.1 Motivation

Recent advances with electromagnetic materials are paving the way to use microwave technology to assist in agricultural development and harvesting [1]. For example, natural silk substrates with edible gold imprints have been proposed as bio-degradable radio frequency identification (RFID) tags. The bio-degradable nature allows the tags to be placed directly on produce (e.g. eggs, tomatoes, etc.). In this application, one could interrogate the RFID tag during different stages of the growing season and determine when the produce is ideal for harvesting.

In this work, it is proposed that the same technology could be used as a non-destructive method to determine if fruit or vegetables are at a specific level of ripeness. Clearly, such a technology would be an aide to the consumer where the consumer would place the RFID tag on the produce and then use a smart device to interrogate the RFID tag to determine the level of ripeness.

The underlying approach is based on the interaction of electromagnetic properties of the produce with the RFID tag. Figure 1 illustrates the concept where the tag is placed on the surface of a watermelon. The tag is designed to resonate at a specific frequency and when placed on the watermelon, the resonant frequency shifts according to the level of ripeness.



Figure 1: Conceptual RFID design

Figure 2 shows a notional curve that is an example of ripeness level versus resonant frequency. The consumer can place the metamaterial RFID tag on different watermelons until one is found that is at the desired level of ripeness. However, there are some significant challenges to designing the RFID tag for this application. As produce contains a significant amount of water and sugars, the produce presents a lossy substrate that inhibits the resonant nature of the RFID tag. Hence, this thesis investigates methods to design a split-ring resonator for use as an RFID tag on a lossy substrate.

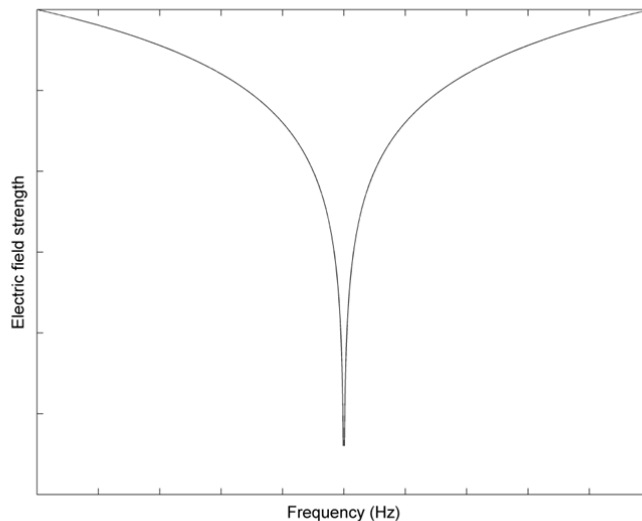


Figure 2: Notional Resonant Curve

The sensitive interaction between organic materials and customized electromagnetic devices is not well understood. Building upon recently reported work using organic split-ring resonators (SRRs), this work proposes an empirical method using full-wave modeling and simulation to study the frequency response of the loaded SRR. The method is put forward by modeling microwave scattering of different SRRs attached to common fruit such as apples and characterizing the resonant frequency shift caused by changing properties of the fruit.

1.2 Challenges

As of now, there is no report on how to use RFID tags to specifically monitor changes in organic materials. One possible concept would be to use RFID transmitters to excite the RFID tag and sense the resonant frequency. As the ripeness and electromagnetic material properties change, the resonant frequency would change as well. There are three main challenges that much be addressed in

order to complete this work. The first challenge is to determine how sensitive the RFID technology is to changes in the resonant frequency. The frequency at which the SRR resonates is based upon the geometry of the device itself. There are five parameters that can be altered within the SRR, each believed to have a unique effect on the resonant frequency. The five parameters are ring width, internal radius, external radius, inner ring spacing, and distance of the splits. SRR alteration options must be well understood in order to develop a sophisticated RFID design to monitor organic material changes.

The second challenge to overcome is the characterization of the material property at different stages of organic growth and decay. The change in the electromagnetic properties of the SRR has a considerable impact on the structures resonant frequency, just as the SRR geometry does. An understanding of how increased dielectric constant and loss affects the resonant frequency will provide insight into how the resonant frequency of an organic substrate changes as it grows and decays.

The knowledge of how the structures resonant frequency is affected by modifying the SRR geometry while also altering the substrates electromagnetic properties is crucial to the research challenge. The overall research challenge is to modify the SRR design to maintain a desired resonant frequency range regardless of the electromagnetic properties of the test subject. With this new technology, one could begin characterizing various organic materials. In the case of produce, the characterization would occur during different stages of growth, harvesting, and ripening.

1.3 Research Hypothesis

The aim of this research is to understand how the SRR can be modified or augmented to build an RFID tag for lossy substrates. The lossy substrate is intended to replicate the properties of common fruits and vegetables. With this

resonant design capability understood, the ability to monitor the changes in selected produce through the cultivation process would then become a possibility.

An electromagnetics modeling and simulation software model is specified with the proper quantities to model an SRR structure attached to a substrate with modifiable electromagnetic properties. The model represents a scattering boundary problem in the far-field domain. This model enables design variation of the SRR geometry and simulation of far-field scattering by the SRR tag.

The primary contribution of this study is a better understanding of how increasing the gap between the rings of a split-ring resonator and increasing the array size improves the resonant response of an SRR when it is placed on a substrate with a small amount of loss (loss factor less than 3). The secondary contribution is the derived resonant frequency equation for an SRR with two rings and four capacitive slits.

Chapter II presents a literature review based on published work related to the SRR and dielectric properties of agriculture. The information is presented in such a way that a general knowledge of electromagnetics is assumed to be possessed by the reader. Chapter III describes the research methodology used for this work and develops an electromagnetic model which is used for the investigation of SRR interaction with high permittivity and lossy substrates. This model is used to provide insight into how to properly alter the SRR geometry based on the permittivity of its substrate. Results are presented in chapter IV and the utility of the results, along with the recommendation for follow up work is discussed in chapter V.

2 Literature Review

2.1 Chapter Overview

This section reviews material regarding current methods for monitoring produce growth, SRR design, electromagnetic properties of common fruits and vegetables, and electromagnetic modeling and simulation of complex objects in lossy media.

The current and emerging methods for monitoring and researching produce growth can be found in [1]. Literature on resonant structures can be found in [3],[4],[5]. These articles provide insight as to which structure is most appropriate to the proposed application. Data regarding the dielectric constant and loss factor of the fruit test subjects used in this work can be found in [6]. This information is required to properly model the interaction between the selected test subject and a resonant structure across a range of frequencies. Literature regarding mathematically modeling electromagnetic interactions and simulating these models can be found in [7]. These engineering techniques provide insight into how to properly create the model and observe the desired scattering phenomena.

2.2 Silk-Based Sensing

An application that is currently in the research phase is fabrication of sub-micron thick gold nano particles and silk substrates to develop a conformable, edible,

ripeness monitoring device [1]. The device acts as a wireless passive antenna that operates over multiple regions of the electromagnetic spectrum [1]. The antenna was tested for functionality by monitoring the resonant responses continuously during the spoilage process to observe the potential changes in food quality. The passive devices can generally be modeled as an LC resonant circuit whose behavior is dependent on both the dielectric properties and geometry of the substrate material. The resonant frequency can be modeled as,

$$f_0 = \frac{1}{2\pi\sqrt{LC}} \quad (1)$$

L is influenced by the geometry of the antenna and C is directly related to the substrate material and surrounding environment. The research hypothesis is similar to that of this work, that the resonant response will be affected by the shift in dielectric constant of the test subject (produce).

2.3 Split-Ring Resonator Design

The enabling technology for monitoring related changes in material properties is the split ring resonator (SRR). The SRR is a device, when measured on a very small scale, appears to have electromagnetic properties that do not occur in nature. The SRR is a composite material that has received growing interest in recent years for its use to construct metamaterials [3]. The size of the SRR's is much less than the wavelength of an incident electromagnetic wave. As a result, the Effective Medium Principle is applicable while working with split ring resonators. The capacitance values and resonant frequencies of multiple SRR designs are calculated using analytical models and numerical simulations in [3]. The SRR's are constructed using non-magnetic concentric copper rings with splits oriented at opposing sides of one another. The planar SRR array is fabricated on FR4 printed circuit boards and units of SRR's are extracted from the array. To observe capacitance, surface mount capacitors are placed at three different capacitive regions of the SRR. These regions include:

- 1) gap region between inner and outer rings
- 2) outer ring split region
- 3) inner ring split region

SSR's are constructed in such a way that they consist of two concentric rings separated by a gap, both having splits oriented on opposite sides. The SRR operates because while current cannot flow around any one ring due to the split separation, the capacitance between the two rings allow the flow of displacement current [8]. SRR's can be modeled as LC circuits in the areas where the inductance arises from the rings. The total capacitance of the system has two main contributions. The first being the capacitance at the split regions and the second from the gap between the two concentric rings. The authors in [3] conducted their experiments in a similar manner as the research effort at hand. The resonant frequencies of the structures were determined by including a layer of SRR structures along the direction of incident plane wave propagation. Open boundary conditions were employed along the propagation direction in the simulation setup. Periodic boundary conditions were used along directions other than that of the incident excitation. Therefore, the structure was assumed to be infinitely periodic along the directions that are perpendicular to the propagation direction. The electric field amplitudes were observed at a distant point from the resonant structure. This point was chosen such that it was far enough away to be affected from arbitrary structural scattering or unwanted attenuation. The choice in point placement was made with the concept in mind that the near field effects should be excluded due to the effects of the structure's highly resonant nature. The theoretical resonant frequency could then be calculated as

$$\omega_n = \frac{1}{\sqrt{L_{av}(\frac{2\pi C}{4} + C_{g11} + C_{g12} + C_{g21} + C_{g22})}} \quad (2)$$

where

L_{AV} = average inductance of the two rings

C = capacitance due to the spacing between the two rings

$C_{g11} + C_{g12} + C_{g21} + C_{g22}$ = capacitances due to the gaps of the inner and outer rings respectively

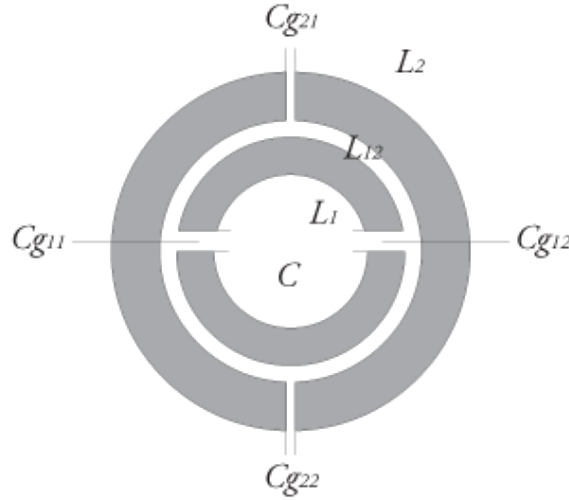


Figure 3: Split-ring resonator electrical parameters.

Figure 4. below shows the resonant structures with electric field excitation

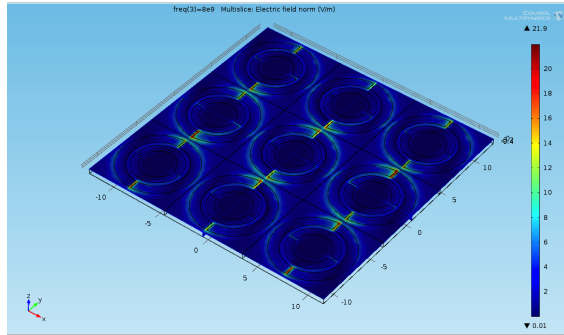


Figure 4: SRR array excited with an 8 GHz plane wave.

Research from [4] found that the majority of the electric field is concentrated at the split region of the outer ring. The other split in the resonant structure contains a small amount of electric field concentration but not nearly to the extent of the outer split region. The paper concludes that when one is concerned with the tune ability or non-linearity of an SRR structure the split region should be considered more importantly than the gap. As the split-width is increased the capacitance decreases

which in turn increases the resonant frequency. While as the gap between the rings is increased the resonant frequency increases due to the reduction of mutual capacitance. Also, as the metal width increases there is a decrease in the mutual inductance and capacitance. Therefore, SRR's with thinner rings have lower resonant frequencies. As a whole, when more capacitance is added to the system the resonant frequency of the system decreases. This relationship is verified in figure 5, where the reflection curves are shown for different ring widths.

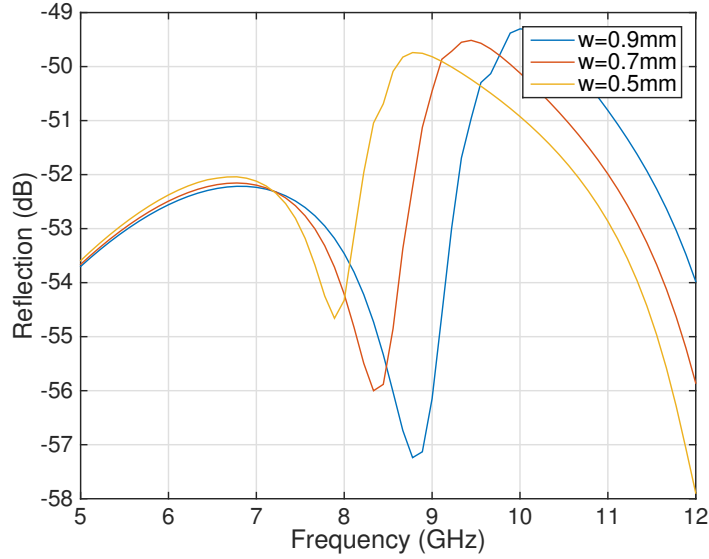


Figure 5: Normalized reflection coefficient vs. frequency for varying gap widths w

2.4 Resonance

A resonator is a device that naturally oscillates at a set of frequencies known as its resonant frequencies. The energy at these frequencies is greater than at other frequencies. In the case of the split-ring resonator, the device stores electromagnetic energy at a specific set of frequencies. The RLC circuit is a classic example of a resonant circuit and the SRR is often modeled with an RLC circuit [5].

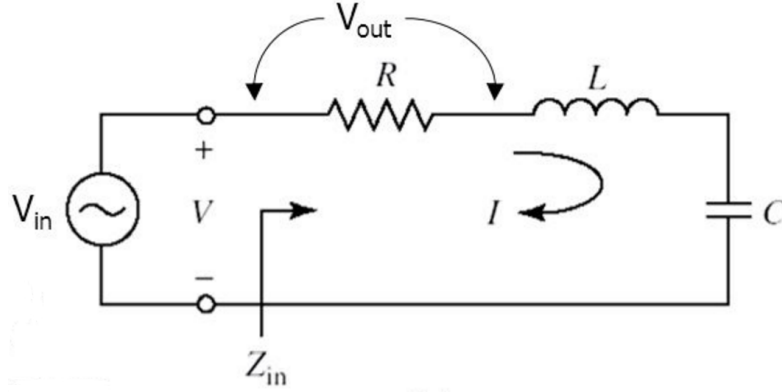


Figure 6: Series RLC circuit from [5]

Following the presentation in [5], the input impedance for a series RLC circuit is

$$Z_{in} = R + j\omega L - j\frac{1}{\omega C} \quad (3)$$

The complex power provided to the circuit is

$$P_{in} = \frac{1}{2}|I|^2(R + j\omega L - j\frac{1}{\omega C}) \quad (4)$$

A certain amount of power is dissipated by the resistor R,

$$P_l = \frac{1}{2}|I|^2 R \quad (5)$$

However, there is an average amount of magnetic energy stored by the inductor L,

$$W_m = \frac{1}{4}|I|^2 L \quad (6)$$

and an average amount of electric energy stored by the capacitor C,

$$W_e = \frac{1}{4}|I|^2 \frac{1}{\omega^2 C} \quad (7)$$

The input impedance can be rewritten as

$$Z_{in} = \frac{P_l + 2j\omega(W_m - W_e)}{\frac{1}{2}|I|^2} \quad (8)$$

From simple circuit theory it is known that stored energy is reactive energy, which

causes resonant behavior. Resonance occurs when the average stored magnetic and electric energies are equal, $W_m = W_e$. When resonance occurs the input impedance is equal to

$$Z_{in} = \frac{P_l}{\frac{1}{2}|I|^2} = R \quad (9)$$

which is a purely real value. The resonant frequency is therefore defined as,

$$\omega_0 = \frac{1}{\sqrt{LC}} \quad (10)$$

A crucial parameter used to define the resonant frequency is the quality factor Q , which is defined as,

$$Q = \omega \frac{\text{average energy stored}}{\text{energy loss/second}} \quad (11)$$

$$Q = \omega \frac{W_m + W_e}{P_l} \quad (12)$$

Q is therefore a measure of the loss in a resonant circuit. Thus, a higher loss implies a lower Q -factor. For the series RLC circuit the Q can be defined as,

$$Q = \frac{1}{\omega_0 RC} \quad (13)$$

and the quality factor decreases as the resistance increases.

The bandwidth can also be defined as a function of the quality factor as

$$BW = \frac{1}{Q} \quad (14)$$

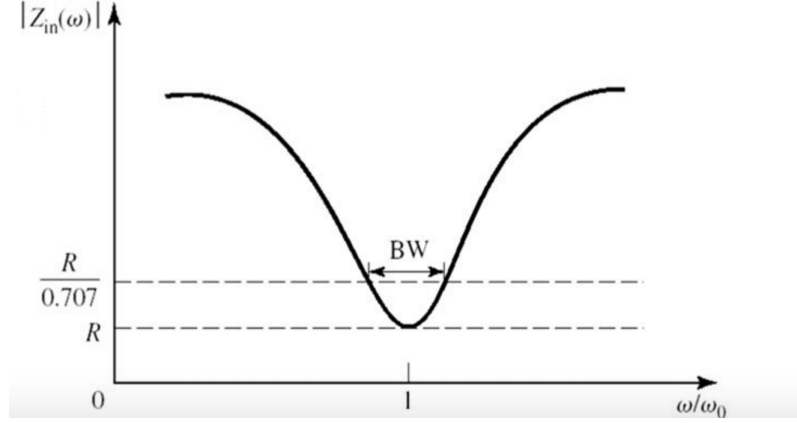


Figure 7: Input impedance magnitude vs. frequency from [5]

2.5 Dielectric Resonant Antenna

The dielectric resonant antenna (DRA) is a microwave component that was first used as a high frequency filter and oscillator. DRA's work well as waveguide cavities due to their small size, high Q factor, temperature control capability, low cost, and flexibility to resonate in different geometries. DRA's operate as antennas and radiate energy most effectively when mounted on top of flat metallic ground planes. The most effective form of excitation to a DRA is by either aperture, microstrip line, or probe coupling. The DRA's performance is a function of feed mechanism, size and shape of the structure, and its material properties [6].

DRA's can take on many different geometries. This study lends attention to the cylindrical DRA due to its structural compatibility with the topic of interest. The resonant frequency of the DRA can be determined at the structures dominant mode, TM_{110} .

The dominant frequency mode is

$$f_{110}^{TM} = \frac{1}{2\pi a \sqrt{\mu\epsilon}} \sqrt{(x'_{11})^2 + \left(\frac{\pi a}{2d}\right)^2} \quad (15)$$

where for this particular mode,

$a = 5.96$ mm (radius of the DRA)

μ is the magnetic permeability of the DRA

ϵ is the electric permittivity of the DRA

$x'_{11} = 1.841$ (mode constant)

$d = 8$ mm (length of the DRA)

Some ways to improve the prominence of resonance of a DRA include: adding an extra dielectric coating to the exterior to improve impedance bandwidth and radiation. Increasing perforations and air gaps will reduce the Q-factor but increase band width. Increasing air gaps has also been shown to increase antenna gain.

Adjusting the circular section of the cylinder will increase the Q-factor, decrease the bandwidth, and create a greater sensitivity to a particular resonance. Knowledge of low-profile and compact attributes give a sense of intuition for an optimal design.

The DRA has negligible metallic loss and as a result it operates at a high efficiency at millimeter wave frequencies. DRA's are made of high permittivity materials with a dielectric constant ($\epsilon_r > 20$). The unloaded Q-factor tends to be between 50 and 500 but can be as high as 10,000. Devices with Q-factors significantly higher than 500 store energy instead of radiating it. The only loss factor for a DRA is due to imperfect material properties, in practice these losses tend to be very small. While adjusting a resonant device to observe produce ripeness is a promising approach, it is worth while to take notice of technologies that are in development to serve the same purpose.

2.6 Utilizing Parallel Plate Capacitance to Determine Banana Ripeness

A method for non-invasively determining the ripeness level of bananas in lieu of direct measurement of its dielectric constant is shown using parallel plate capacitors in [11]. According to Maxwell's equations, the dielectric constant of a material is a key factor in determining the velocity in which an electromagnetic wave propagates. Prior to this work, the current methods for measuring fruit ripeness included firmness teasing using penetrometer or impact force, measuring pH levels and

measuring parameters such as sugar and ethanol. While these parameters provide insight into ripeness levels to an extent, these methods all require destruction of the test subject and complex analytical techniques. Some complex non-destructive methods include nuclear and proton magnetic resonance detection. These experiments are conducted by placing ripened and unripened bananas between capacitive plates with fixed geometries and applied peak-to-peak voltages. The results found in [11] are such that an increased plate separation will decrease the capacitance of both ripe and unripe bananas at different rates until they are at an equal 10-cm separation. The authors in [12] found that green-ripe bananas have a higher permittivity than the fully ripened ones. Through experimentation it was found that a quadratic regression had a higher prediction power than a linear regression. It was also found that the best frequency to observe permittivity fluctuations was at 1 MHz. The green ripe bananas dielectric constant equal to 1.7433 dropped to 1.6931 during a five day ripening process. The experiment used the same approach as [11]. Using parallel plate capacitances and a banana test subject, the non-linear regression plot created from the research found that the permittivity decreased as the frequency increased. There are reports that the sugar content was up twenty percent by day six of ripening. It was found that there is a high correlation between the banana permittivity and quality. The sensing system of [11] was developed at 1 MHz because there is a visible correlation between firmness and sugar content with relative permittivity at this frequency.

2.7 Dielectric Properties of Fruit

Several studies regarding dielectric characterization were carried out in the past forty years with two of the leading contributors being Nelson and Venkatesh. These studies investigated fruit, vegetables, grain, and seed. Nelson investigated the dependence between dielectric properties and temperature, moisture content, and frequency. The feasibility of using dielectric properties to sense the quality of these products.[13],[14] and [15]. Nelson studied dielectric properties of watermelon and found correlations between soluble solid content as a factor of fruit [15] and [17].

Ragni employed dielectric properties of egg to predict quality parameters in [18] and Sirikulrat demonstrated that the relative permittivity of the fresh soybean decreases as the bean matures [19]. All of these research efforts were fundamental approaches and a necessity for future understanding but were not anywhere near becoming a practical application.

The research by Nelson [20] found that a parameter to test for honey dew melon quality is solubility, which is due mostly to sugars and is a measure of how sweet a melon is. For this work, honey dew melons were grown and harvested with a range of maturities and soluble solid contents with the intention to learn whether differentiating dielectric property values could be correlated with quality or “ripeness”. Testing was performed using dielectric spectroscopy measurements. The experimentation was done by extracting tissue samples from the melons and measuring its soluble solid content (SSC) with an SSC calibrated refractometer. Experiments were conducted in the frequency range of 100 MHz to 1.8 GHz and all measurement samples were taken by making a 3-cm thick equilateral slice on the melons. There were 6 samples total, half for moisture content measurement and the other half for measuring the dielectric content. Results were found by studying the correlation between dielectric properties and SSC’s of the thirty eight melons tested and eight frequencies within the predetermined range were selected for observation.

Nelson investigated the ripening effects over a ten week period with respect to the dielectric properties. It was found that over the ten-week storage process the apple’s dielectric properties stayed relatively constant even though the firmness of the apple’s decreased significantly. When SSC was used as the quality factor in correlation with permittivity it was found that the dielectric constant and loss factor correlations were low. There was a high correlation between SSC and permittivity found from a complex plane analysis of the dielectric constant and loss factor each divided by SSC, however, quality prediction from the relationship was not very high.

Table 1: Dielectric fruit properties from [9], $\text{real}(\epsilon_r)$

Material	Moisture Content %	0.2 GHz	0.5 GHz	1.3 GHz	3.2 GHz	8 GHz	20 GHz
GD (apple)	86.5	63.4	61.9	60.2	57.0	46.1	28.4
GS (apple)	88.4	58.3	57.8	56.3	53.3	43.5	26.9
RD (apple)	87.3	58.1	57.3	55.6	52.8	42.9	24.8
Banana	78.1	0.94	66.3	63.0	57.5	43.7	24.9
Grapefruit	91.5	0.83	76.6	73.9	72.3	57.9	33.8
Lemon	91.2	0.88	74.5	71.7	70.3	57.8	34.3
Orange	87.5	0.92	74.8	71.2	68.0	51.7	29.2

Table 2: Dielectric Fruit properties from [9], $\text{imag}(\epsilon_r)$

Material	Moisture Content %	0.2 GHz	0.5 GHz	1.3 GHz	3.2 GHz	8 GHz	20 GHz
GD (apple)	86.5	16.0	9.8	8.3	13.2	21.8	26.0
GS (apple)	88.4	17.2	9.8	8.0	12.3	20.4	24.7
RD (apple)	87.3	16.7	9.7	7.9	12.2	20.6	25.4
Banana	78.1	56.92	27.8	17.6	19.0	25.9	23.1
Grapefruit	91.5	38.0	18.6	12.3	16.4	27.8	30
Lemon	91.2	44.9	21.2	12.9	15.1	27.3	29.6
Orange	87.5	33.5	17.7	13.2	17.7	28.4	27.8

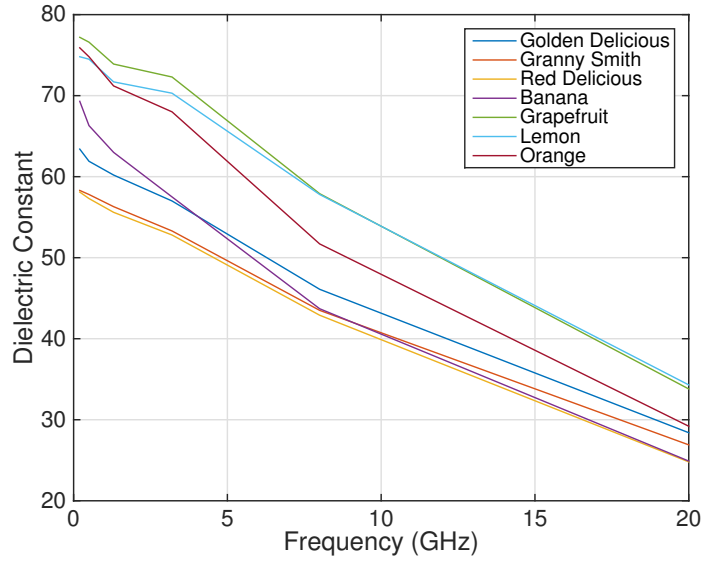


Figure 8: Dielectric constant as a function of frequency from [9].

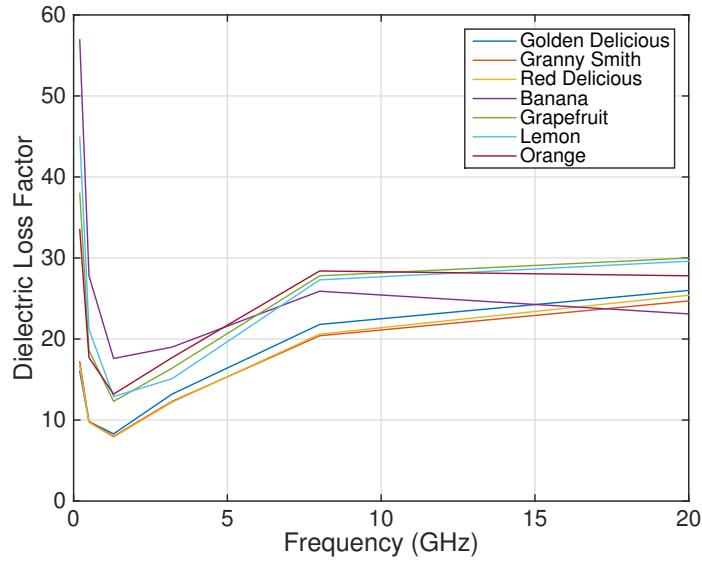


Figure 9: Dielectric loss factor as a function of frequency from [9].

2.8 Electromagnetic Modeling and Simulation

Electromagnetic modeling and simulation enables the study of a wide variety of issues ranging from microwave scattering to antenna design. Topics of interest also include radio wave propagation, wireless communication, radar surveillance systems and more. Devices have sizes ranging from small scale (nano meters) to large scale (kilometers wide) and operate from the direct current range all the way up to the terahertz range. A majority of these devices are broadband digital and operate within close proximity of one another which as a result is a catalyst for a whole host of electromagnetic interference issues.

The proposed engineering analysis is largely done with electromagnetic modeling and simulation software that solves Maxwells equations for a specified set of boundary conditions. Commercial products such as FEKO and Comsol are used in each stage of development from design, analysis, implementation, and testing. Electromagnetic simulation requires high powered computational hardware and software that is capable of solving applied mathematics and physics problems in the form of complex electromagnetic boundary problems that cannot be solved by

means of analytical methods. When using modeling and simulation tools, users face the challenge of assigning correct parameters such as certain assumptions, frequency bandwidth, material properties, geometry details, the amplitude of excitation signals and so on.

Once the model's geometrical and physical properties are properly defined, further decision is required pertaining to the electromagnetic solver method utilized in the problem. The decision as to what solver method to use is crucial to the solution. As the solver method's computation time and accuracy, and depend on the geometries size and complexity, some problems can not be solved at all. Some commonly used solver methods include Method of Moments (MoM), Finite Difference Time Domain (FDTD), Physical-Optics (PO), Uniform Theory of Diffraction (UTD), Ray-Launching (RL), and the Finite Element Method (FEM) [23].

MoM is a numerical approximation technique used to solve electric and magnetic field integral equations. Basis functions for the unknown quantity change the integral equation into a matrix equation which can be solved. Alternatively, FDTD discretizes Maxwell's equations by replacing derivatives with their finite difference approximations directly in the time domain. Due to computer memory limitations, the near field is typically found and the far fields are extrapolated from the near fields. PO is an approximation that uses ray optics to estimate specular reflections that include diffraction effects. UTD is used for high frequency scattering problems. It approximates the near field and uses ray diffraction to determine coefficients for each diffraction object-source combination. RL is similar to PO and is used for high frequency scattering problems. It approximates the far-field and uses ray tracing to approximate multiple arbitrary numbers over singular and multiple reflectors.

2.9 Finite Element Method in Comsol Multiphysics®

The Finite Element Method (FEM) is most appropriate to the problem in this study. Like the other methods, FEM is a numerical technique used for finding

approximate solutions to boundary problems for partial differential equations. It divides the problem into smaller subsets and as a result more simplified portions referred to as finite elements. FEM uses methods that connect many simple element equations over discretized finite elements, to approximate a more complex equation over an entire domain [24].

It is advantageous to use FEM due to its accurate representation of complex geometry, its inclusion of dissimilar material properties and its capture of local effects. Some difficulties of using FEM as a solver include the large matrix and need to transform near field solutions to far field solutions. FEM for electromagnetics involves specifying Maxwell's equations and boundary conditions for the entire problem domain. Given the different material properties, the problems divided into sub-domains. The FEM formulation simultaneously solves Maxwell's equations in all of its sub-domains. The process involves constructing a weighted integral and minimizing the residual. The process is essentially a procedure that minimizes the error caused by basis approximation of the unknown in the PDE. The FEM is well documented for arbitrary electromagnetics problems [24].

2.10 Comsol Multiphysics[®]

Comsol Multiphysics uses FEM to solve for electromagnetic fields within the modeling domain under the assumption that the fields are time harmonic at a known angular frequency, $\omega = 2\pi f$, and that all material properties are linear with respect to field strength. The source free wave equation is

$$\nabla \times (\mu_r^{-1} \nabla \times \vec{E}) - \frac{\omega^2}{c^2} (\epsilon_r - \frac{i\sigma}{\omega\epsilon_0}) \vec{E} = 0 \quad (16)$$

where,

μ_r = relative permeability

ϵ_r = relative permittivity

σ = electric conductivity

$c =$ the speed of light in a vacuum

$\omega = 2\pi f$ where f is the operating frequency

The above equation is solved for the electric field $\vec{E} = \vec{E}(x, y, z)$ throughout the modeling domain where \vec{E} is a vector component with $\vec{E} = \hat{x}E_x + \hat{y}E_y + \hat{z}E_z$. The magnetic field can be derived from the electric field [23].

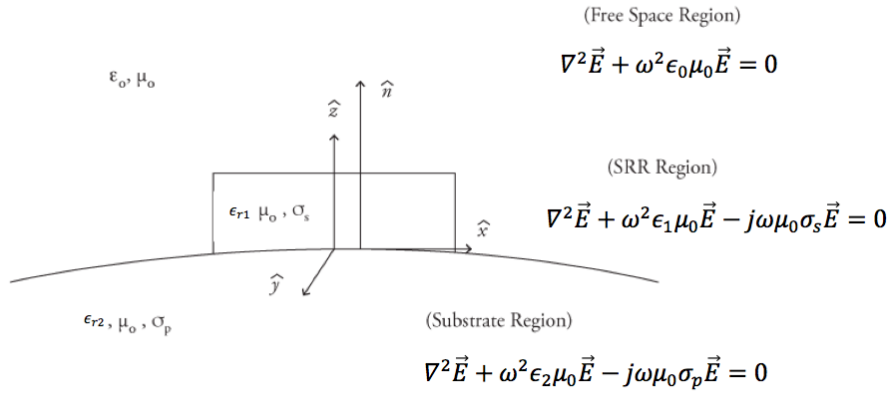


Figure 10: Geometry for boundary conditions and wave equations for each material.

Figure 10 is a side view representation of the boundaries implemented in Comsol. Wave equations in Fig 10. are solved simultaneously. Using a modeling and simulation tool (Comsol) is essential to solving such a large set of differential equations.

The four key steps of modeling and simulation include the model setup which involves defining the equations that need to be solved, creating the model geometry, defining the material properties, and setting up the boundary conditions. The meshing step requires discretizing the model space using FEM. The software then solves a set of linear equations that describe the electric field. The final step, post processing is where the user extracts the needed information from the electric field solutions.

3 Methodology

3.1 Chapter Overview

The question of “How can an SRR operate on a lossy substrate?” is presented to help define the problem of this thesis. Based on this inquiry, the research hypothesis is postulated because it is necessary to declare not only a motivation for why to collect data but also an organizational structure.

Research Hypothesis

An SRR system in this work is defined as an SRR structure attached to a substrate with a specific thickness and material property. When loss is introduced to the system, the resonant behavior cannot be sustained without modification to the system. It is possible to mitigate the loss in resonant frequency by adjusting the SRR’s geometric parameters.

3.2 Analysis Method

This research hypothesis can be tested by experimentation. The most time efficient and cost effective analysis method in this case is modeling and simulation. The electromagnetic modeling and simulation will be done in Comsol Multiphysics. The electromagnetic material properties of the test subject will be utilized from the open literature. The SRR design will be constructed based on the frequency of interest

and will be modeled after SRR designs found in the open literature.

A deterministic model will be created in the modeling and simulation environment to accurately verify the resonant frequency shift of the system as a function of each SRR parameter as it corresponds to the open literature. Once verification has been achieved the model will then be analyzed and a relationship will be drawn for the resonant frequency shift as a function of the systems loss. Experimentation will take place once the device's properties are understood with respect to resonant frequency and resonant frequency as a function of substrate loss has been verified. The experimentation will observe how SRR parameters can be altered to maintain a resonant frequency within a lossy system.

SRR parameters for this work include: the parameter split width d , the gap distance g , metal width w , radius outer ring r_1 and radius inner ring r_2 as illustrated in Fig 11.

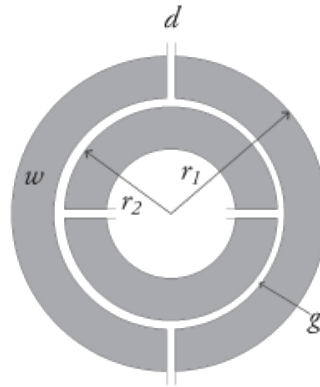


Figure 11: Split-ring resonator parameters.

The SRR structure consists of two concentric circular rings made of a perfect electric conductor (PEC). In the experiment the structure is excited by a time varying electric field that is incident perpendicularly to the plane of the SRR. When

excited, a current flow is induced along the rings. This current flow is solenoidal (meaning that the divergence of the current is zero everywhere), therefore the SRR can be considered as a resonant magnetic dipole. The SRR stores energy by concentrating the incident electric field within the gap between its rings. The structures will be simulated in a 3x3 array which can be considered a reflectarray. The incident wave in the simulation is a plane wave with unit amplitude 1 V/m

3.3 Split-Ring Resonator Equivalent Circuit Model

An equivalent circuit model for an SRR with two rings and a single gap per ring was created by [26].

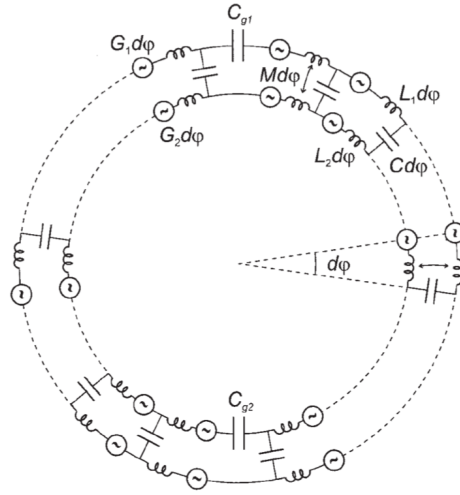


Figure 12: SRR equivalent circuit model from [26].

While this is an accurate representation of this particular design, the SRR structure used in this work not only contains gaps at $\varphi = \frac{\pi}{2}$ and $\varphi = -\frac{\pi}{2}$ but also at $\varphi = 0$ and $\varphi = \pi$

A closed form equation for the lowest resonant frequency is derived in [26]. In the discussion below, this derivation will be modified to include the additional gaps.

Applying Kirchoff's current law to a $d\varphi$ current element the differential equations

$$-\frac{\partial y}{\partial \varphi} = I_1 j\omega(L_1 - L_{12}) - I_2 j\omega(L_2 - L_{12}) + G_2 - G_1 \quad (17)$$

$$\frac{\partial I_1}{\partial \varphi} = -j\omega CV \quad (18)$$

$$\frac{\partial I_2}{\partial \varphi} = j\omega CV \quad (19)$$

where ω is the angular frequency, V_1 is the inner ring, I_1 and I_2 are the currents on the inner and outer rings, C is the inner ring capacitance, G_1 and G_2 are the induced voltages, L_1 and L_2 are the inductances of rings 1 and 2, and L_{12} is the mutual inductance between them.

The angular variable φ extends from $-\pi$ to π . The four gap capacitances C_{g11} , C_{g12} , C_{g21} and C_{g22} are located at $\varphi = \frac{\pi}{2}$, $\varphi = -\frac{\pi}{2}$, $\varphi = 0$ and π respectively, which divides the SRR into four separate regions. The differential equations must be written to individually represent each region. There are six boundary conditions that are then applied. After much reduction that can be found in [25], the resonant frequencies can then be obtained by the following characteristic equation

$$\begin{aligned} &\kappa[\sin(\kappa\pi[4\pi\kappa^2 - \pi\gamma_1\gamma_2\gamma_3\gamma_4 - 2(\gamma_1 + \gamma_2)V_2 - 2(\gamma_3 + \gamma_4)V_1]) \\ &+ \cos \kappa\pi[\gamma_1\gamma_2\gamma_3\gamma_4(V_1 + V_2) - 2\pi\kappa^2(\gamma_1 + \gamma_2 + \gamma_3 + \gamma_4)]] = -2\gamma_1\gamma_2\gamma_3\gamma_4\sqrt{(V_1V_2)} \end{aligned} \quad (20)$$

where,

$$\kappa^2 = \omega^2 L_{eq} C$$

$$\gamma_1 = \frac{C}{C_{g11}}$$

$$\gamma_2 = \frac{C}{C_{g12}}$$

$$\gamma_3 = \frac{C}{C_{g21}}$$

$$\gamma_4 = \frac{C}{C_{g22}}$$

$$V_1 = \frac{L_1 - L_{12}}{D}$$

$$V_2 = \frac{L_2 - L_{12}}{D}$$

$$L_{eq} = L_1 + L_2 - 2L_{12}$$

and

$$D = \sqrt{L_1 L_2 - L_{12}^2}$$

Assuming that κ is much smaller than unity and the trigonometric functions can be

expanded, the term L_{12} drops out from the lowest resonant frequency

$$\omega_1 = \sqrt{\frac{1}{L_{av}(\frac{2\pi C}{4} + C_{g11} + C_{g12} + C_{g21} + C_{g22})}} \quad (21)$$

where

$$L_{av} = \frac{L_1 + L_2}{2}$$

3.4 Wave Equation in a Lossy Medium

The primary source for this derivation is [8].

$$\vec{D} = \epsilon \vec{E} \quad (22)$$

The electric flux \vec{D} is polarized with the electric field \vec{E} for isotropic medium, where the permittivity ϵ is complex valued. The time harmonic version of Maxwell's equation is

$$\nabla \times \vec{H} = \vec{J} + j\omega \vec{D} \quad (23)$$

where \vec{J} is the electric current density and is made up of two parts. \vec{J}_i which is the impressed current (an excitation by an outside source) and the conduction electric current \vec{J}_c (caused by the application of an external electric field), such that

$$\nabla \times \vec{H} = \vec{J}_i + \vec{J}_c + j\omega \vec{D} \quad (24)$$

However, $\vec{J}_c = \sigma_s \vec{E}$ where σ_s is the conductivity of the background medium; and

$$\nabla \times \vec{H} = \vec{J}_i + \sigma_s \vec{E} + j\omega \vec{D} \quad (25)$$

When an external electric field is applied, the dipoles align in the material with the field, causing a term to be added to the electric flux density that has the same vector direction as the applied field.

$$\vec{D} = \epsilon_0 \vec{E} + \epsilon_0 \chi_e \vec{E} \quad (26)$$

χ_e is the electric susceptibility which serves as a scalar constant between the applied electric field and the portion of the electric flux density caused by the presence of the dielectric.

$$\vec{D} = \epsilon_0(1 + \chi_e)\vec{E} \quad (27)$$

$$\text{or } \vec{D} = \epsilon_0\epsilon_r\vec{E}$$

where ϵ_r is the relative permittivity of the medium

In most cases ϵ_r is a complex quantity and the conduction current is combined with the displacement current. therefore,

$$\nabla \times \vec{H} = \vec{J}_i + \sigma_s\vec{E} + j\omega(\epsilon_0\epsilon_r)\vec{E} = \vec{J}_i + j\omega(\epsilon' - j\epsilon'')\vec{E} \quad (28)$$

Then

$$\nabla \times \vec{H} = \vec{J}_i + (\sigma_s + j\omega\epsilon_0\epsilon_r)\vec{E} = \vec{J}_i + j\omega(\epsilon' - j\epsilon'')\vec{E} \quad (29)$$

and

$$\sigma_s + j\omega\epsilon_0\epsilon_r = j\omega\epsilon_0\epsilon_r\left(1 - j\frac{\sigma_s}{\omega\epsilon_0\epsilon_r}\right) = j\omega\epsilon'\left(1 - j\frac{\epsilon''}{\epsilon'}\right) \quad (30)$$

where

$$\epsilon' = \epsilon_0\epsilon_r \quad (31)$$

and

$$\frac{\epsilon''}{\epsilon'} = \tan\delta_e \quad (32)$$

therefore the imaginary part of relative permittivity is directly related to the system loss. The total permittivity can be modeled as

$$\epsilon_0\epsilon_r = \epsilon' - j\epsilon'' \quad (33)$$

and the loss tangent can be defined as

$$\tan\delta_e = \frac{\sigma_e}{\omega\epsilon'} \quad (34)$$

therefore

$$\nabla \times \vec{H} = \vec{J}_i + j\omega\epsilon'(1 - j\tan\delta_e)\vec{E} \quad (35)$$

The loss tangent describes how much energy supplied by an external electric field is dissipated by internal dipole rotation.

For a metal such as the PEC material used for the SRR structure, the effective loss is almost entirely due to the collision of electrons. Therefore, the second term is dropped

$$\nabla \times \vec{H} = \vec{J}_i + (j\omega\epsilon_0\epsilon_r + \sigma_s)\vec{E} \quad (36)$$

The substrate material attached to the SRR is a dielectric. The effective loss for a dielectric is due almost entirely to polarization loss, which is caused by dipole motion and can be represented as

$$\nabla \times \vec{H} = \vec{J}_i + j\omega\epsilon'(1 - \frac{\epsilon''}{\epsilon'})\vec{E} \quad (37)$$

Now, the wave equation for a plane wave traveling in a medium that is conductive, source free, weakly dispersive (the permittivity varies slowly with frequency), isotropic, and homogeneous, is

$$\nabla^2 \vec{E} + \omega^2\mu\epsilon'(1 - j\tan\delta_e)\vec{E} = 0 \quad (38)$$

3.5 Model Validation

In order to verify the validity of the SRR model created in Comsol it must be tested against other collected simulation data sets. For this purpose the results from [25] shown in Figure 13 will be reproduced. The starting SRR parameters for this verification are $d = g = 0.2$ mm, $w = 0.9$ mm and $r = 3.6$ mm. The split width d will then vary from $d = 0.2$ mm to $d = 0.5$ mm in a 0.1 mm step size.

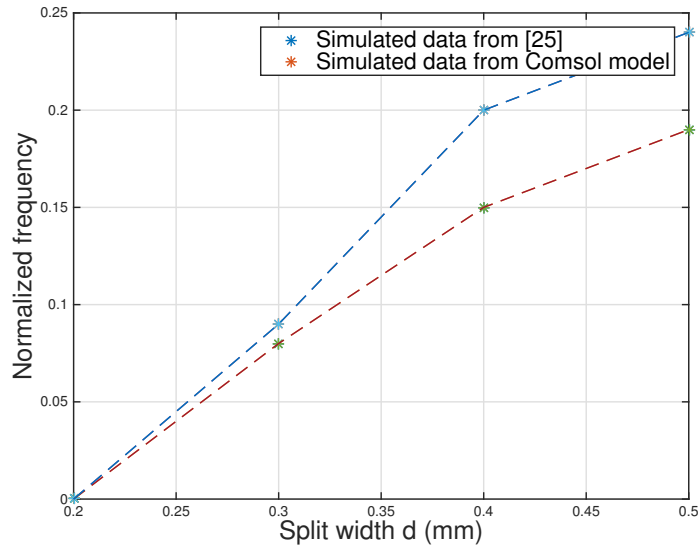


Figure 13: Split width d vs. normalized frequency with simulated data and data from [25].

Notice that the normalized frequencies are much lower in the model results than in [25], this behavior is due to the geometry and permittivity of the substrate being different in each case. Since the substrate parameters are not listed in [25], the design for the model's substrate is created with $\epsilon_r = 1 - 0j$ and a square plate that is 8 mm in length, 8 mm in width, and 0.5 mm in thickness. The verification is valid because each case observes an increase in resonant frequency as the parameter split width d increases.

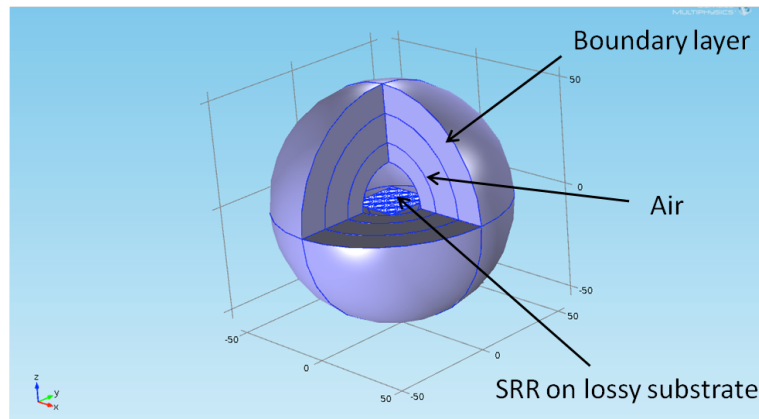


Figure 14: SRR model created in Comsol Multiphysics®.

Figure 15 shows the model created for this experiment. Each layer of the sphere encasing the SRR array serves a specific purpose. The inner most layer is free space,

then as the domain expands outward there is a far field boundary layer and a perfectly matched layer defined to attenuate unwanted reflected signals resulting from the finite computational domain.

4 Results

4.1 Results

In order to confirm that the model is in fact resonating at the frequency to which it is tuned, the SRR array is attached to a substrate with the permittivity of free space $\epsilon_r = (1 - 0j)$. The reflected electric field strength is normalized to that reflected from a flat plate of $\frac{|E_s|^2 A^2}{\lambda^2}$. The substrate for this model is an 8 mm by 8 mm square. What will be referred to as the standard SRR design for this thesis is $g = d = 0.2$ mm , $r_2 = 2.5$ mm, $r_1 = 3.6$ mm and $w = 0.9$ mm. The standard configuration is displayed in Figure 15. The reflected and transmitted signals for the standard SRR design placed on a free space substrate is compared with substrates of increasing permittivity. The reflected signal is observed directly above and centered on the SRR structure and the transmitted signal is observed directly below and centered. An outline of chapter 4's many sections and subsections is listed below.

Subsection 4.1.1 presents results for substrates with an increasing dielectric constant, subsection 4.1.2 presents results of a substrate with an increasing loss factor and subsection 4.1.3 presents results for a highly lossy substrate. Section 4.2 presents the SRR parameter changes in this study with 4.2.1 presenting results for a changing gap distance g , subsection 4.2.2 presenting results for 3 split rings, subsection 4.2.3 displaying results for a changing split width d , 4.2.4 displaying results for a changing ring width w , and subsection 4.2.5 summarizing the results. The focus of section 4.3 is the effect that the SRR array size has on resonance with 4.3.1 being the effects of array size on a standard SRR and section 4.3.2 involves

increasing the gap width on a 4x4 array.

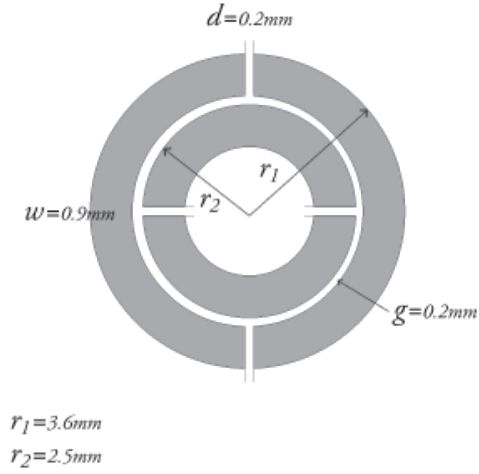


Figure 15: Standard SRR configuration

4.1.1 Results for a lossless substrate

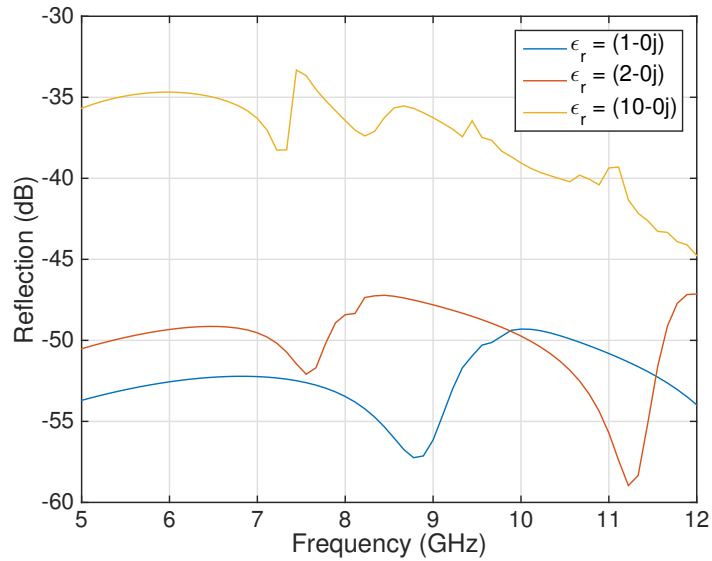


Figure 16: Normalized SRR reflection vs. frequency with increasing dielectric constant of substrate.

The standard SRR configuration is first placed on a substrate with dielectric constant $\epsilon_r = (1 - 0j)$. The results are in agreement with the frequency that the

SRR is designed to resonate at. The SRR is then placed on a substrate with dielectric constant $\epsilon_r = (2 - 0j)$. It is observed that there is an increase in the resonant frequency as the permittivity increases, which is an expected behavior. The second resonant dip now appears because of the increasing shift as well. The dielectric constant of the substrate is further increased to $\epsilon_r = (10 - 0j)$. The resonant frequencies have now shifted higher than 12 GHz and are no longer observable on the 5-12 GHz axis.

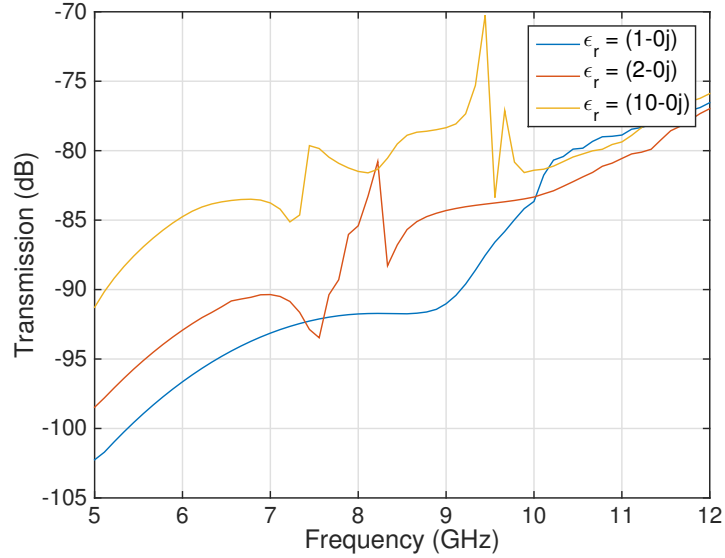


Figure 17: Normalized SRR transmission vs. frequency with increasing dielectric constant of substrate.

The transmission results agree with the SRR's resonant behavior at all substrate dielectric constants that the structure is placed on. The transmission is expected to be very weak, as all energy incident to the SRR is either reflected or is resonating within the structure. There is a large spike in the transmission signal for the substrate $\epsilon_r = (10 - 0j)$ that is assumed to be a solver error at that particular frequency.

4.1.2 Results for a lossy free space substrate

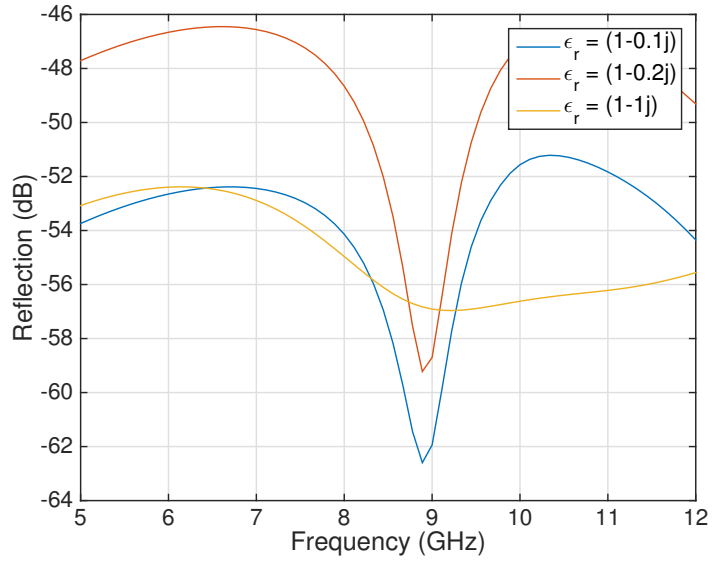


Figure 18: Normalized SRR reflection vs. frequency with increasing substrate loss factor.

The SRR is now observed on a substrate with a small amount of loss introduced to the system ($\epsilon_r = 1 - 0.1j$). Resonance is maintained when observing the reflection. The substrate loss is then increased to $\epsilon_r = (1 - 0.2j)$. There does not seem to be much of an affect on the resonant frequency other than a slight decrease in the resonant dip. It is observed from the reflected signal that increasing the substrate loss to $\epsilon_r = (1 - 1j)$ causes the resonant behavior to dissipate, which motivates the experiment towards changing SRR parameters with the intent of maintaining resonance on a substrate with a higher loss factor.

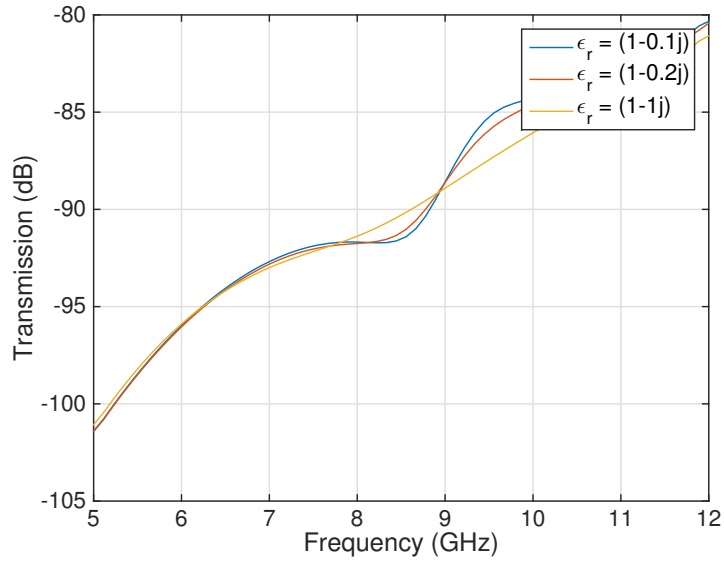


Figure 19: Normalized SRR transmission vs. frequency with increasing substrate loss factor.

The transmission results agree with the SRR’s resonant behavior at all substrate loss factors that the structure is placed on. The transmission is expected to be very weak, as all energy incident to the SRR is either reflected or is resonating within the structure.

4.1.3 Results for a highly lossy dielectric substrate

While it is crucial to understand how to tune an SRR given a lossless dielectric substrate, this tuning has already been investigated by papers such as [27] and is therefore outside the scope of this thesis.

The primary interest for this thesis is to find how to properly tune an SRR design to maintain a resonant frequency when attached to a lossy substrate. The goal is to design an SRR that can maintain a resonant frequency in the X-band (between 8 to 12 GHz) while attached to a substrate with loss as high as a golden delicious apple ($\epsilon'' = 26$). The experiment begins by first placing the SRR on a substrate simulating free space $\epsilon_r = (1 - 0j)$ and comparing it to an SRR placed on a substrate with a minimal amount of loss $\epsilon_r = (1 - 0.1j)$.

It is known that the increased real part (ϵ') permittivity of a substrate has a direct correlation with the resonant frequency and field intensity [27]. This concept is verified for the model by changing the substrate from $\epsilon_r = 1 - 0j$ to $\epsilon_r = 2 - 0j$.

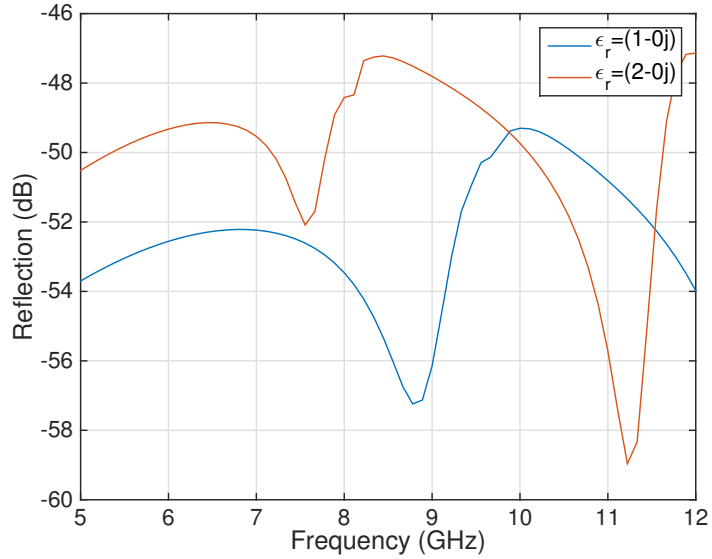


Figure 20: Normalized SRR reflection vs. frequency with increasing substrate $\text{real}(\epsilon_r)$.

and from $\epsilon_r = 10 - 0j$ to $\epsilon_r = 20 - 0j$

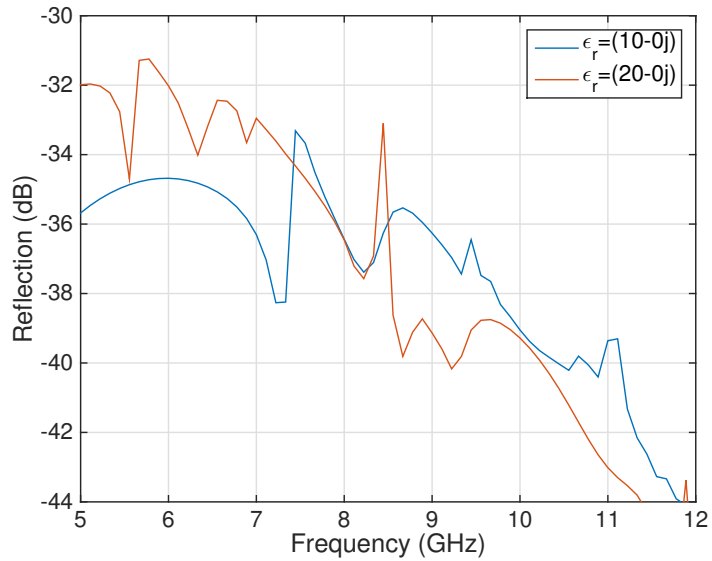


Figure 21: Normalized SRR reflection vs. frequency with increasing substrate $\text{teal}(\epsilon_r)$

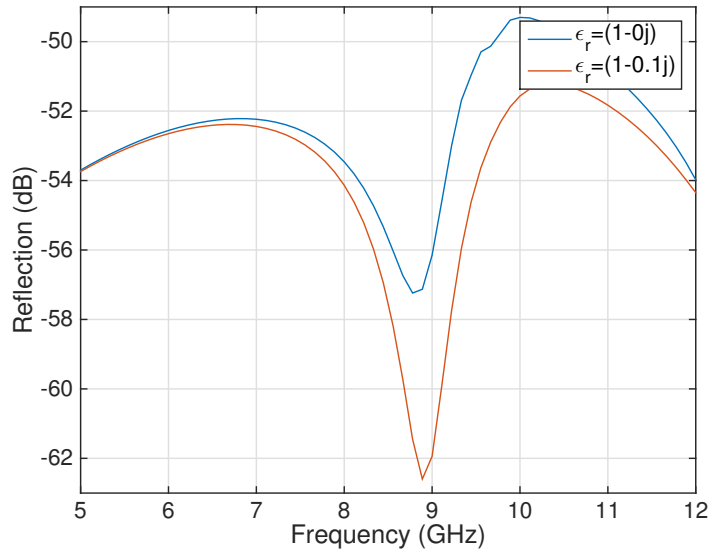


Figure 22: Normalized SRR reflection vs. frequency with increasing substrate $\text{imag}(\epsilon_r)$

It appears that introducing a small amount of loss to the substrate actually increases the functionality of the SRR structure. This seems reasonable as SRR's are typically designed to be placed on imperfect substrates that contain small amounts of loss such as circuit board silicon material and ceramics. As the loss continues to increase,

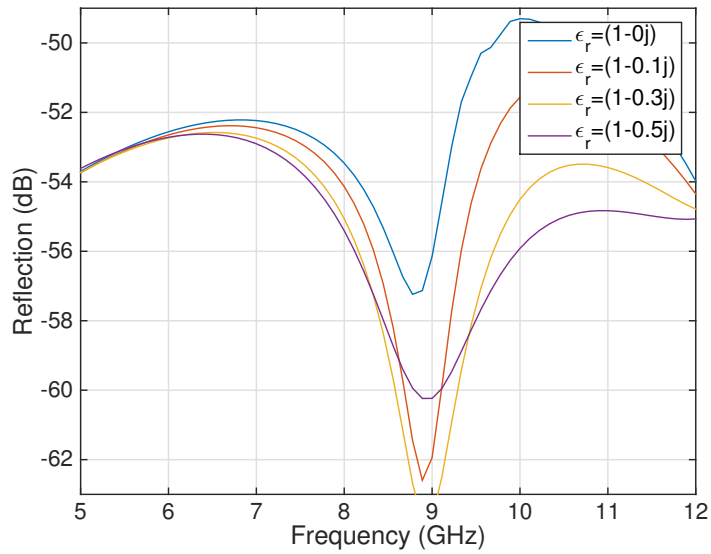


Figure 23: Normalized SRR reflection vs. frequency with increasing substrate $\text{imag}(\epsilon_r)$

it becomes clear that between $\epsilon'' = 0.3$ and $\epsilon'' = 0.5$ the resonant behavior is lost.

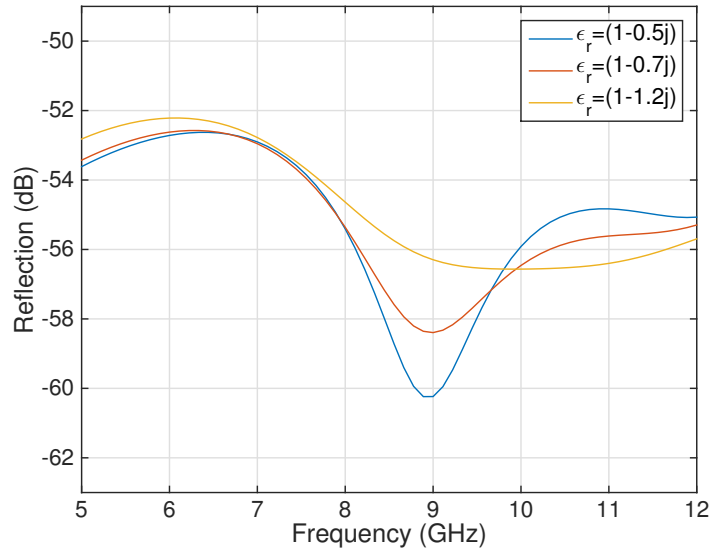


Figure 24: Normalized SRR reflection vs. frequency with increasing substrate $\text{Imag}(\epsilon_r)$

When $\epsilon'' > 1.2$ the SRR structure can no longer maintain any sort of resonant behavior. newline

4.2 SRR Parameter Changes

4.2.1 Results for changing gap distance g

It is known from [3] that increasing the gap distance g between the two rings of the SRR structure decreases the mutual capacitance and mutual inductance between the rings, thus increasing the resonant frequency of the system. Assuming that increasing the resonant frequency of the SRR structure will increase its ability to maintain resonance on a lossy substrate, an experiment is set up that increases gap distance g on a substrate with permittivity $\epsilon_r = (1 - 0.5j)$.

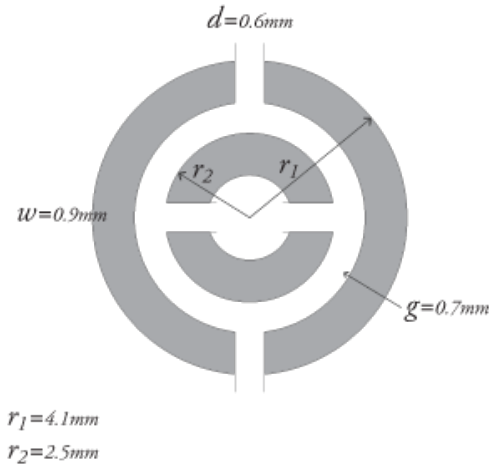


Figure 25: SRR configuration with increased gap distance g .

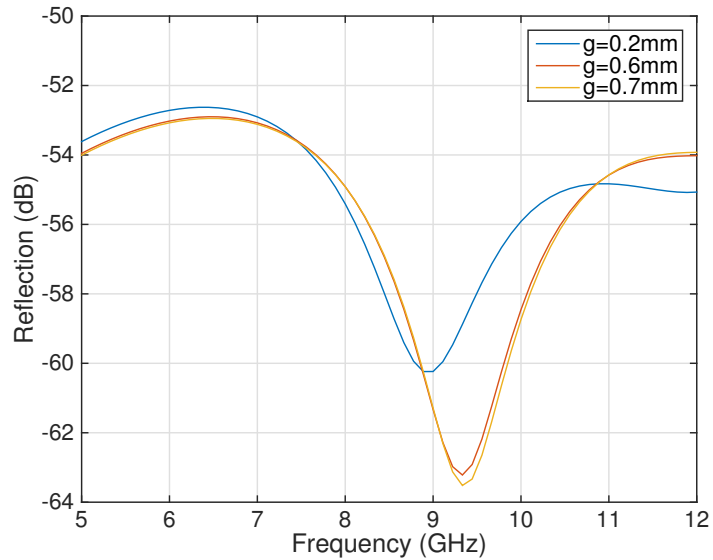


Figure 26: Normalized SRR reflection vs. frequency with increasing gap distance g .

The results in Figure 26 show that while the resonant frequency is in fact increased, the SRR structure also maintains a more prominent dip in resonance (-63.5 dB) on a substrate with $\epsilon'' = 0.5$ compared to when it had its standard design and was attached to a substrate with $\epsilon'' = 0$ (-57 dB). Figure 35 also implies that while a much more prominent dip in resonance is obtained when g increases from 0.2 mm to 0.6 mm, the results are much less prominent when increasing g from 0.6 mm to 0.7

mm. To obtain a better understanding of this phenomenon, the permittivity is then increased to $\epsilon_r = (1 - 1j)$ and the gap values are increased from $g = 0.6$ mm to $g = 0.7$ mm. The results are shown in Figure 27.

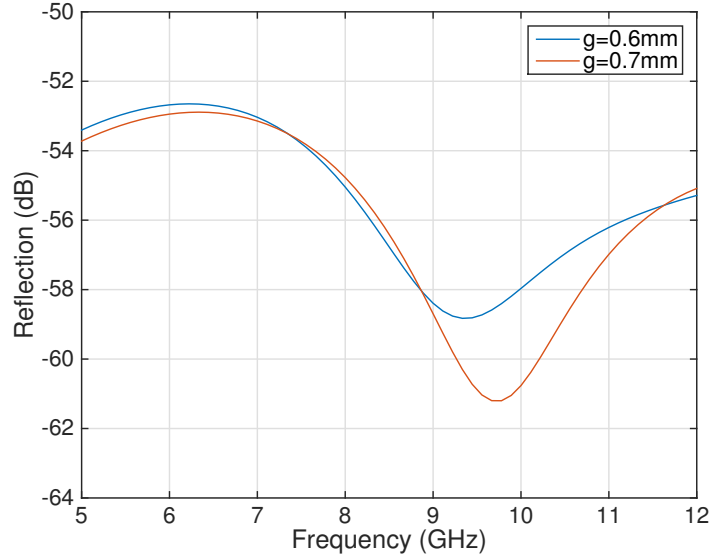


Figure 27: Normalized SRR reflection vs. frequency with increasing gap distance g .

While there is a small effect for the gap increase between $g = 0.6$ mm to $g = 0.7$ mm when the substrate permittivity is $\epsilon_r = (1 - 0.5j)$, the 0.1 mm gap increase for permittivity $\epsilon_r = (1 - 1j)$ is crucial to maintaining resonance. Figure 28 observes the reflected field strength as ϵ'' increases from 0.5 to 1.0 while the gap is increased from 0.6 mm to 0.7 mm.

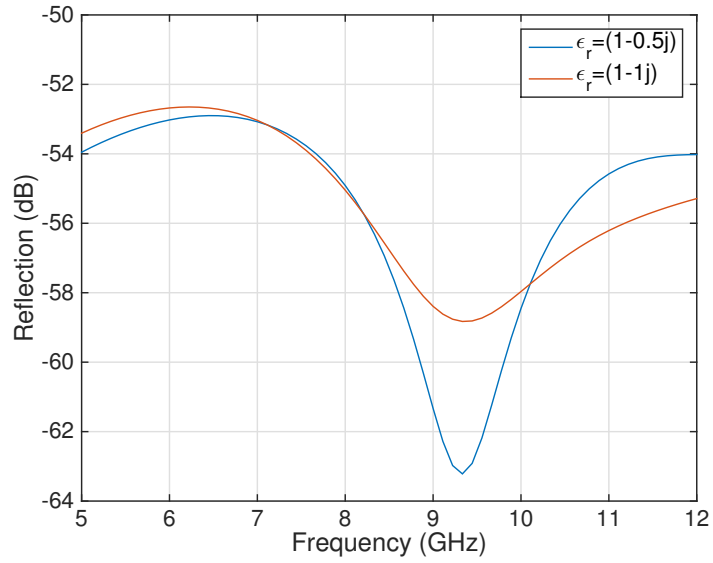


Figure 28: Normalized SRR reflection vs. frequency with increasing substrate $\text{imag}(\epsilon_r)$ and $g = 0.7$ mm.

It is apparent that the SRR structure can no longer maintain resonance when $\epsilon_r = (1 - 1j)$ with a gap value of 0.6 mm. When observing the same change in loss with a gap value of 0.7 mm.

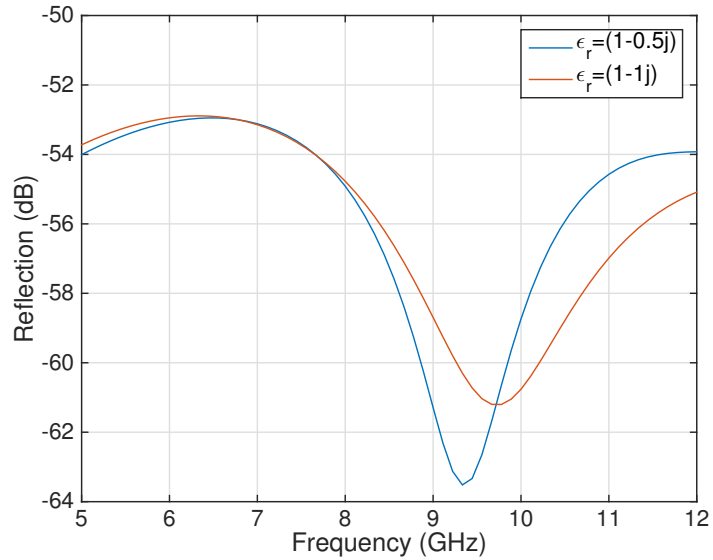


Figure 29: Normalized SRR reflection vs. frequency with increasing substrate $\text{imag}(\epsilon_r)$ and $g = 0.9$ mm.

It is clear that the 0.1-mm gap increase is crucial to maintaining resonance for a

substrate of $\epsilon_r = (1 - 1j)$. This relationship between increasing the gap value and maintaining the resonant frequency at increasing loss values leads one to believe that significantly increasing the gap width will cause the resonant frequency to be increased but maintained at a significantly higher loss value. Fig 30 displays the reflection curves for $g = 1.2$ mm and the loss increasing from $\epsilon'' = 2.5$ to $\epsilon'' = 3.0$.

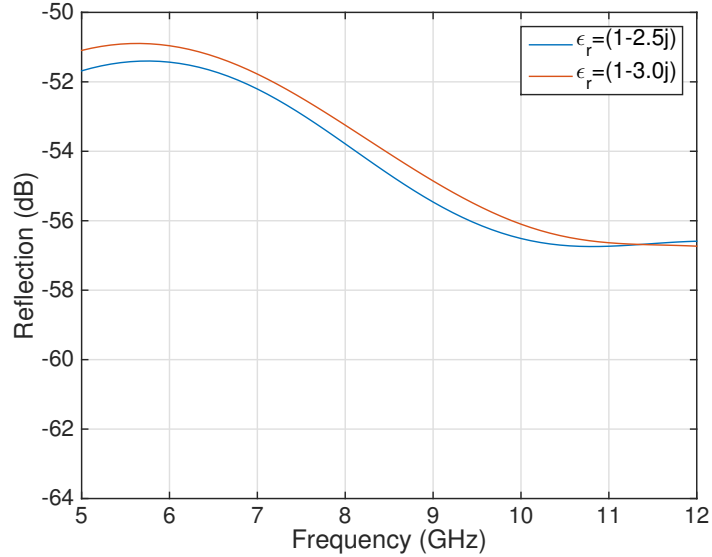


Figure 30: Normalized SRR reflection vs. frequency with increasing substrate $\text{imag}(\epsilon_r)$.

It is clear that if the loss of the substrate is going to be increased to a significant amount, the SRR structure must be modified from its original configuration in ways other than just the gap width. It also raises the question as to whether or not increasing the gap width is only useful to a certain extent.

With $\epsilon_r = (1 - 3j)$ at its highest value investigated thus far in the study, the gap is further increased to investigate if it truly has reached a saturation point.

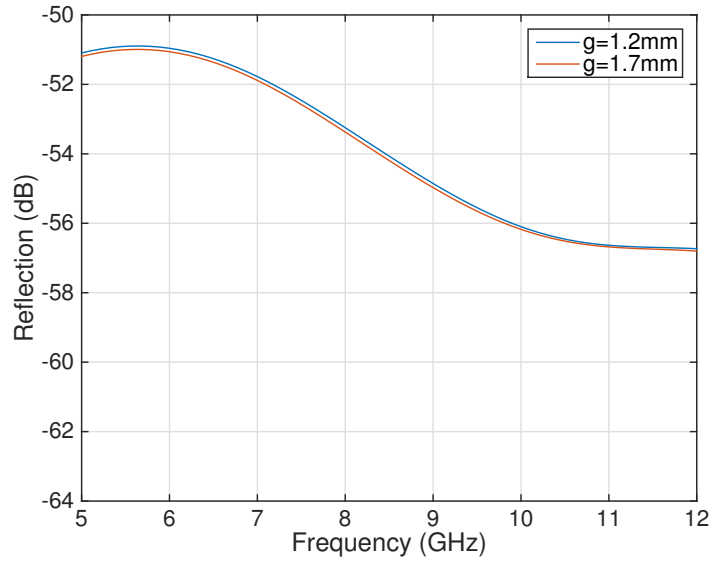


Figure 31: Normalized SRR reflection vs. frequency with increasing gap distance g .

This proves that increasing the gap is in fact not going to be the only parameter that needs to be altered for this study.

4.2.2 Results for three split rings

It is worth going back to a lower loss value to observe if other changes in the SRR structure is going to be able to maintain a resonance as the loss of the substrate increases. While it is not documented in [3], the assumption is made that increasing a third, smaller ring with the same slit widths within the SRR structure may decrease the mutual capacitance and mutual inductance, thus increasing the resonant frequency. Results are shown in Figure 33.

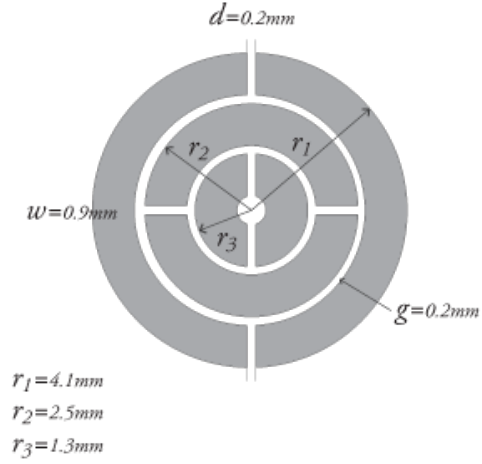


Figure 32: SRR configuration with third inner ring

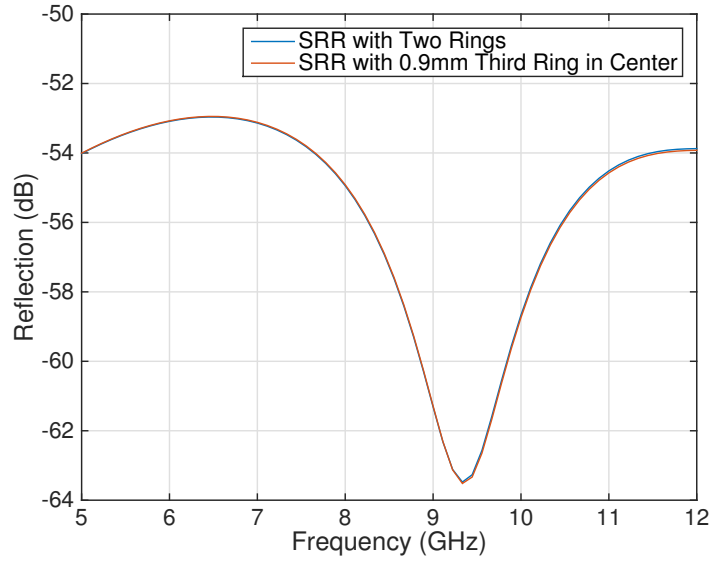


Figure 33: Normalized SRR reflection vs. frequency with third inner ring.

This assumption proved to be incorrect, as it is clear that adding an additional third ring that is 0.9 mm in radius has no effect on the resonant frequency compared with the standard SRR configuration.

4.2.3 Results for changing split width d

Another parameter to observe is the split width d . A study in [3] shows that

increasing d increases the resonant frequency by decreasing the overall capacitance of the system. Since increasing the gap width g has already proven successful to an extent, the gap width will be fixed at $g = 0.7$ mm, the permittivity of the substrate will be fixed at $\epsilon_r = (1 - 1j)$, and the split width d will be increased.

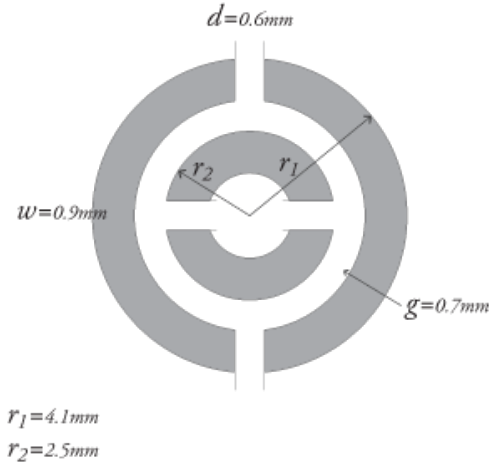


Figure 34: SRR configuration with increased split width d and increased gap distance g .

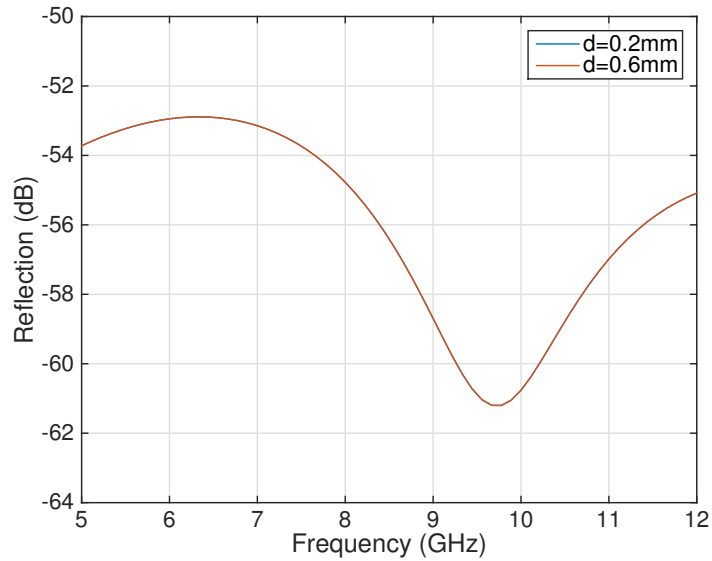


Figure 35: Normalized SRR reflection vs. Frequency with increasing split width d .

While d does provide an increase in the resonant frequency value with the standard SRR configuration and a lossless substrate, it is in a saturation region if the gap is

greater than the standard configuration gap, $g = 0.2$ mm and there is a lossless system.

4.2.4 Results for changing ring width w

Another parameter that is studied in [3] is the metal width w . As the radius of the inner ring increases there is a decrease in the mutual inductance and mutual capacitance in the system, which causes an increase in the resonant frequency. Therefore, SRR's with thinner rings will have a lower resonant frequency. This study explores how the resonant frequency is effected by a decreasing inner ring radius if the gap g is fixed at 0.6 mm.

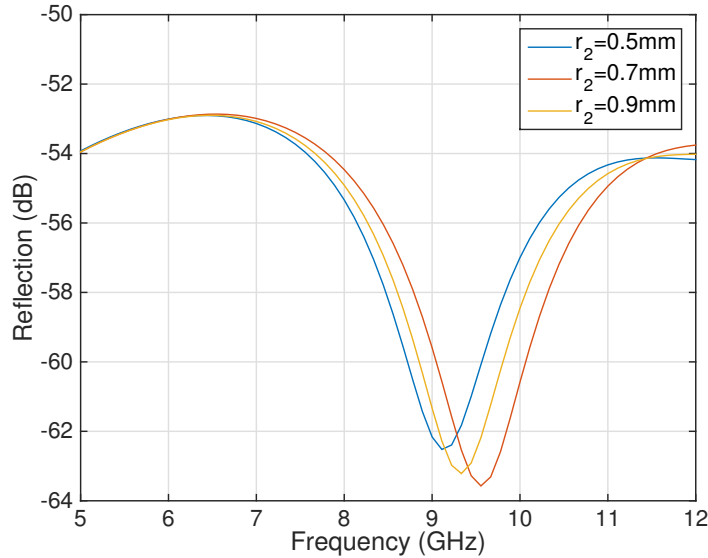


Figure 36: Normalized SRR reflection vs. frequency with decreasing inner ring width r_2 .

Figure 36. shows that while decreasing the inner ring radius decreases the resonant frequency when the SRR structure is in its standard configuration. The direct relationship does not exist if the gap g is greater than the standard configuration gap of $g = 0.2$ mm. Since there does not appear to be a tangible relationship between changing the inner gap radius and the resonant frequency, this parameter will not be further investigated.

While it is clear that $g = 1.2$ mm is past its saturation region when $\epsilon_r = (1 - 3j)$,

the outer ring radius is increased in hopes of decreasing the resonant frequency and having a positive effect on the resonant response.

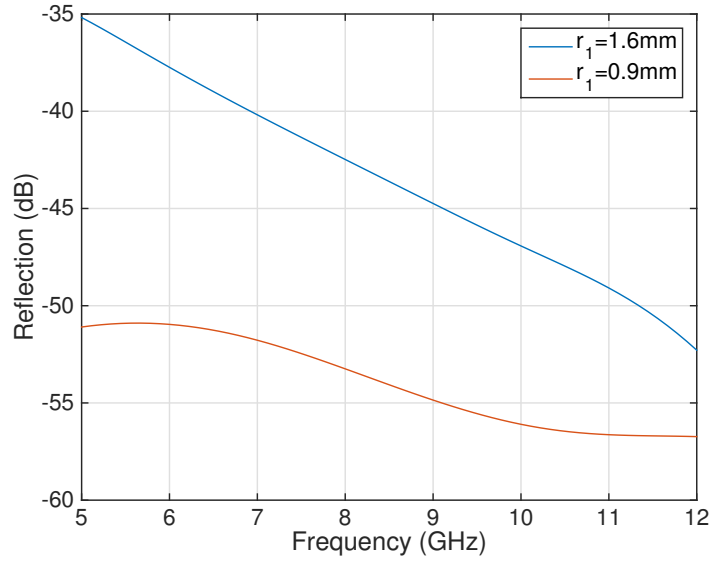


Figure 37: Normalized SRR reflection vs. frequency with increasing outer ring width r_1 .

4.2.5 Summary of geometric changes

It appears that while the SRR configuration is already in saturation, the resonant response shows no improvement when the outer ring radius is increased. With the permittivity $\epsilon_r = (1 - 3j)$, an additional parameter to investigate is the thickness of the substrate. It is reported in [27] that increasing the thickness of the substrate causes the resonant frequency to decrease but makes no mention of this phenomenon when the substrate is lossy.

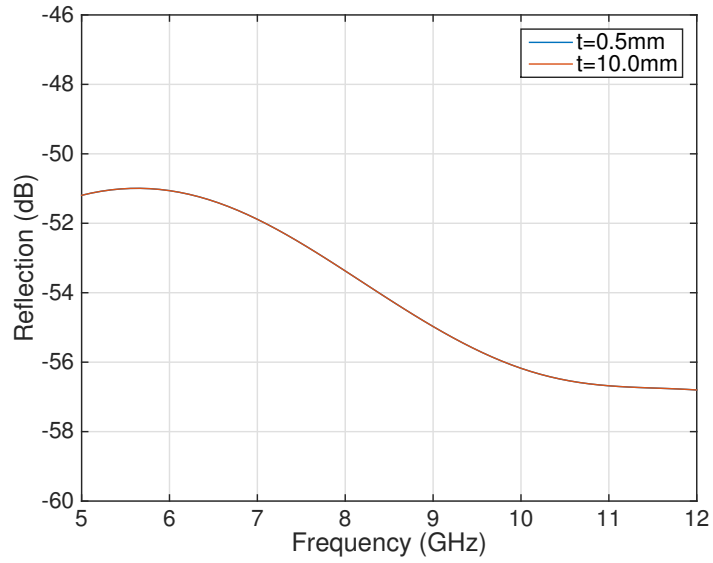


Figure 38: Normalized SRR reflection vs. frequency with increasing substrate thickness t .

It is found that changing this SRR parameter has no effect on the resonant frequency when the substrate has the permittivity $\epsilon_r = (1 - 3j)$.

If the outer ring radius is increased with a smaller gap between rings g , that has proven to not be past the saturation region ($g = 0.8$ mm), there is interest to observe if the SRR structure can mention any resonant frequency with an increased outer ring radius.

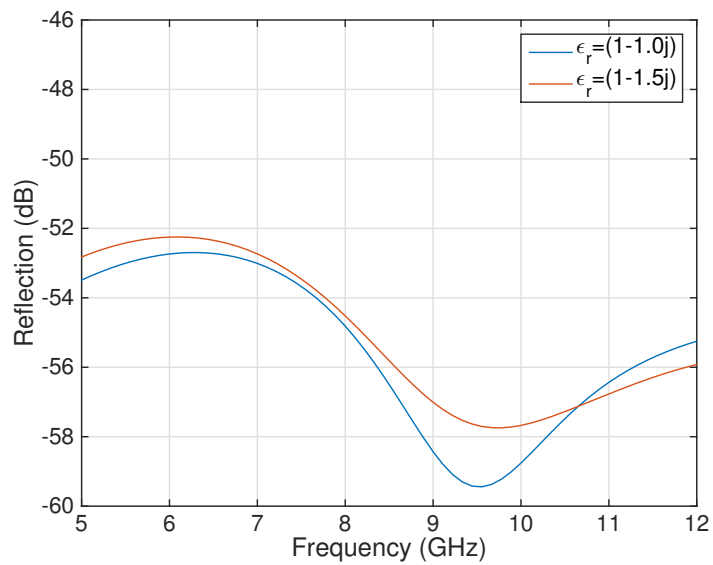


Figure 39: Normalized SRR reflection vs. frequency with increasing substrate $\text{imag}(\epsilon_r)$.

This shows that while increasing the outer ring radius is not useful with the structure parameters $\epsilon_r = (1 - 3j)$ and $g = 1.2$ mm, the outer ring radius change may be useful when altered in tandem with other parameters in a future study. An additional parameter to investigate is the array size.

4.3 Array Size Effects on Resonance

4.3.1 Effects of array size on a standard SRR

Thus far in this study the SRR structure has been a 3x3 array. With a permittivity $\epsilon_r = (1 - 1j)$ and a gap size $g = 0.7$ mm, the array size is increased from 3x3 to 4x4. Results are shown in Figure 40.

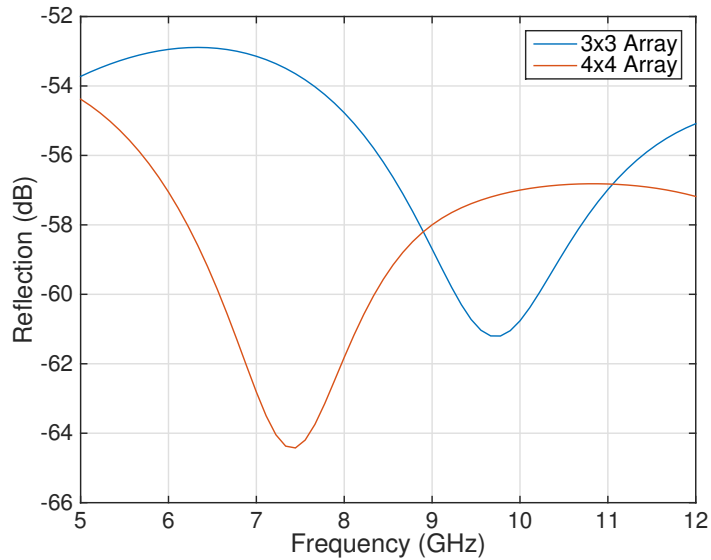


Figure 40: Normalized SRR reflection vs. frequency with increasing array size.

Increasing array size appears to increase the resonant effect observed as a decrease in reflection from and decreased bandwidth. This change does however cause an unwanted shift in the resonant frequency from roughly 9.8 GHz to 7.3 GHz.

Increasing the array size appears promising to increasing the resonance, thus the same structure but with a gap $g = 0.6$ mm is observed on a substrate $\epsilon_r = (1 - 3j)$. The results are shown in Figure 41.

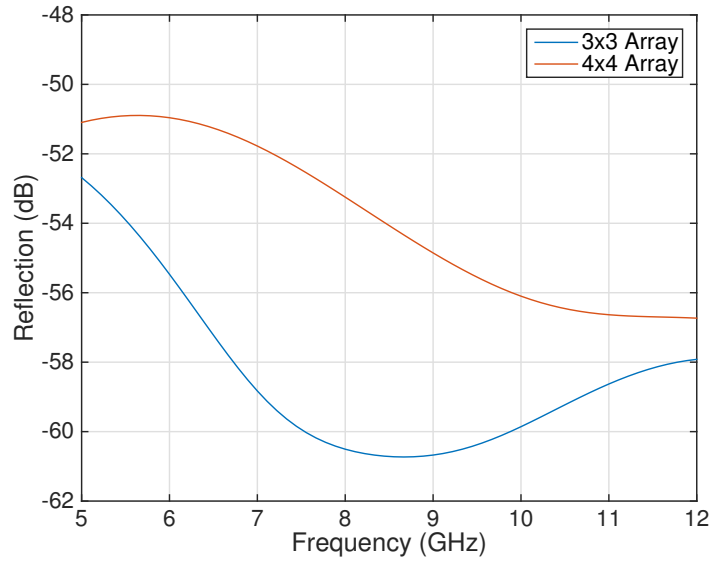


Figure 41: Normalized SRR reflection vs. frequency with increasing array size and $\epsilon_r = (1 - 3j)$.

The 4x4 configuration shows promise in maintaining resonance. Increasing the gap width has been found to increase the resonant frequency even on a substrate $\epsilon_r = (1 - 3j)$. The gap will now be further increased on the 4x4 Array.

4.3.2 Increasing the gap width on a 4x4 array

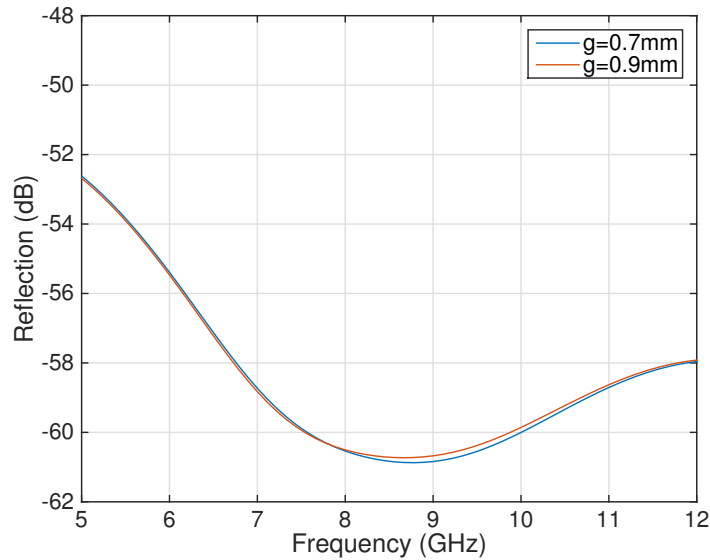


Figure 42: Normalized SRR reflection vs. frequency with increasing gap distance g .

This configuration appears to be somewhat successful at producing a resonant

frequency on a substrate with loss $\epsilon'' = 3.0$. The gap can not be increased past $g = 0.9$ mm as this study has found that it causes the SRR structure to saturate on a high loss substrate.

The logical next step would be to create a resonant structure with $g = 0.9$ mm, $w = 0.9$ mm, $d = 0.2$ mm, $r_1 = 2.7$ mm and $r_2 = 3.6$ mm on a 5x5 array and a substrate with a thickness $t = 0.5$ mm and permittivity $\epsilon_r = (1 - 3j)$.

5 Conclusion and Future Work

5.1 Summary

This thesis showed that it is possible for the baseline SRR to operate on a substrate with an electromagnetic loss factor up to 3.0. The experiment also shed light on what parameters of an SRR can be altered to maintain resonance as the electromagnetic loss of its substrate increases. It was found that increasing the gap width between the two rings, g , has a positive impact on the resonant behavior as it is increased from 0.2 mm to 0.9 mm. It appears that values greater than 0.9 mm have a negative on the systems resonance.

Other techniques used to reduce the SRR's capacitance while on a lossy substrate proved to be less effective. This includes altering the inner and outer ring width w and the split width d . Increasing the array size from 3x3 to 4x4 in conjunction with increasing the gap width to $g = 0.9$ mm proved to maintain the most prominent resonant behavior on the substrate with the loss observed in this experiment ($\epsilon_r = (1 - 3j)$).

The primary contribution of this study is the increased understanding of how altering the SRR design parameters affects the resonant frequency of the SRR when the SRR is placed on a highly lossy substrate. As common fruits have highly lossy electromagnetic properties, the SRR resonance is expected to suffer. It may be possible to maintain the resonance by increasing the array size which could limit the types of fruit for monitoring. The secondary contribution is the derivation of the resonant frequency equation for an SRR with two rings and four capacitive slits.

5.2 Recommendation for Future Work

Computation power limited the array size for this experiment, preventing runs with an array size of 5×5 from completing. The next experiment to continue this work would be to attempt a 5×5 SRR array with $g = 0.9$ mm, $d = 0.2$ mm, $w = 0.9$ mm, $r_1 = 3.6$ mm, $r_2 = 2.5$ mm and placed on a substrate with $\epsilon_r = (1 - 3j)$. If the increased array size is more effective at maintaining resonance on the lossy substrate, the next suggestion would be to continue to increase the array size and increase the substrate loss to test the SRR's true limitations when operating on a lossy substrate. However, one must consider alternative electromagnetics modeling and simulation software so the size of the numerical problem is not a limiting factor in the study.

REFERENCES

- [1]H. Tao, M. Brenckle, M. Yang, J. Zhang, M. Liu, S. Siebert, R. Averitt, M. Mannoer, M. McAlpine, J. Rogers, D. Kaplan and F. Omenetto, 'Food Sensors: Silk-Based Conformal, Adhesive, Edible Food Sensors (Adv. Mater. 8/2012)', *Adv. Mater.*, vol. 24, no. 8, pp. 993-993, 2012.
- [2]R. Rolle, G. Mrema and P. Soni, 'A Regional Strategy for Sustainable Agricultural Mechanization. Sustainable Mechanization across Agri-Food Chains in Asia and the Pacific region', *1st ed. Oceania, Asia: FAO Regional Office for Asia and the Pacific, 2015*, pp. 1-8.
- [3]K. Aydin and E. Ozbay, 'Capacitor-loaded split ring resonators as tunable metamaterial components', *J. Appl. Phys.*, vol. 101, no. 2, 2007.
- [4]M. Durn-Sindreu, J. Naqui, F. Paredes, J. Bonache and F. Martn, 'Electrically Small Resonators for Planar Metamaterial, Microwave Circuit and Antenna Design: A Comparative Analysis', *Applied Sciences*, vol. 2, no. 4, pp. 375-395, 2012.
- [5]D. Pozar, *Microwave engineering*. Hoboken, NJ: J. Wiley, 2005.
- [6]K. Luk and K. Leung, *Dielectric resonator antennas*. Baldock, Hertfordshire, England: Research Studies Press, 2003.
- [7]M. Saed, 'Measurement of the complex permittivity of low-loss planar microwave substrates using aperture-coupled microstrip resonators', *IEEE Transactions on Microwave Theory and Techniques*, vol. 41, no. 8, pp. 1343-1348, 1993.
- [8]C. Balanis, *Advanced engineering and electromagnetics*. Hoboken, N.J.: Wiley, 2011.

- [9] S. O. Nelson, W. R. Forbus, Jr. and K. C. Lawrence, 'Microwave Permittivities of Fresh Fruits and Vegetables from 0.2 to 20 GHz', *Transactions of the ASAE*, vol. 37, no. 1, pp. 183-189, 1994.
- [10] L. Sevgi, 'Electromagnetic Modeling and Simulation: Challenges in Validation, Verification, and Calibration', *IEEE Transactions on Electromagnetic Compatibility*, vol. 56, no. 4, pp. 750-758, 2014.
- [11] M. Soltani, R. Alimardani and M. Omid, 'Prediction of Banana Quality During Ripening Stage Using Capacitance Sensing System', *Australian Journal of Crop Science, AJCS* vol. 4, no. 6, pp. 443-447, 2010.
- [12] Zulhusin, A. Hallis, A. Aziz, R.B. Ahmad, 'Feasibility Study of a Non-Destructive Fruit Maturity Testing System on Banana Utilizing Capacitive Properties', *2008 International Conference on Electronic Design*, 2008.
- [13] V. Mane, V. Puri, 'Microwave Conductivity and Permittivity of Moisture Laden Soybean Seed', *Microwave and Optical Technology Letters*, 2008.
- [14] S.O. Nelson, L.H. Soderholm, and F.D. Yung 'Determining the Dielectric Properties of Grain', *Agricultural Engineering*, 1953
- [15] S.O. Nelson, 'Dielectric Properties of some Fresh Fruits and Vegetables at Frequencies of 2.45 to 22 GHz', *Transactions of the ASAE* pp. 613-613, 1983.
- [16] W.R. Tinga, S.O. Nelson, 'Dielectric Properties of Materials for Microwave Processing', *J. Microwave*, 1973.
- [17] S.O. Nelson, S. Trabelsi, 'Factors Influencing the Dielectric Properties of Agricultural and Food Products', *Journal of Microwave Power and Electromagnetic Energy* 46(2), 2012.
- [18] S.O. Nelson, S. Trabelsi, 'Dielectric Spectroscopy Measurements on Fruit, Meat, and Grain', *Transactions of the ASABE* pp. 1829-1834, 2008.

- [19]L. Ragni, J. Tang, 'Quality Evaluation of Shell Eggs During Storage using a Dielectric Technique', *Transactions of the ASABE* pp. 1331-1340, 2008.
- [20]S. O. Nelson, S. Trabelsi and S. J. Kays, 'Dielectric Spectroscopy of Melons for Potential Quality Sensing', *Transactions of the ASABE*, vol. 51, no. 6, pp. 2209-2214, 2008.
- [21]Stuart O. Nelson, 'Microwave Dielectric Properties of Fresh Fruits and Vegetables', *Transactions of the ASAE*, vol. 23, no. 5, pp. 1314-1317, 1980.
- [22]S. Nelson, W. Guo and S. Trabelsi, 'Investigation of Dielectric Sensing for Fruit Quality Determination', *IEEE Sensors Applications Symposium*, 2008.
- [23]W. Frei, 'COMSOL Multiphysics ® Modeling Software', Comsol.com, 2015. [Online]. Available: <http://www.comsol.com>. [Accessed: 11- Oct- 2015]
- [24]J. Jin, *The finite element method in electromagnetics*. New York: John Wiley & Sons, 2002.
- [25]K. Aydin, I. Bulu, K. Guven, M. Kafesaki, C. Soukoulis and E. Ozbay, 'Investigation of magnetic resonances for different split-ring resonator parameters and designs', *New Journal of Physics*, vol. 7, pp. 168-168, 2005.
- [26]M. Shamonin, E. Shamonina, V. Kalinin and L. Solymar, 'Resonant frequencies of a split-ring resonator: Analytical solutions and numerical simulations', *Microwave and Optical Technology Letters*, vol. 44, no. 2, pp. 133-136, 2004.
- [27]J. Chen, W. Chen, J. Yeh, L. Chen and C. Wang, 'COMPARATIVE ANALYSIS OF SPLIT-RING RESONATORS FOR TUNABLE NEGATIVE PERMEABILITY METAMATERIALS BASED ON ANISOTROPIC DIELECTRIC SUBSTRATES', *Progress In Electromagnetics Research M*, vol. 10, pp. 25-38, 2009.